Materials Advances

ROYAL SOCIETY OF CHEMISTRY

PAPER

View Article Online
View Journal | View Issue

Cite this: *Mater. Adv.*, 2025, **6**, 1478

A family of zinc compounds of an anthracene-appended new multifunctional organic scaffold as potent chemotherapeutics against cervical cancer†

Sujan Sk,[a] Arnob Chakrovorty,[b] Asmita Samadder [b] and Manindranath Bera *[a]

A family of biologically active novel zinc(II) compounds, namely [Zn(ahpa)(Cl)(H_2O)] (**1**), [Zn(ahpa)(NO_3)(H_2O)] (**2**) and [Zn(ahpa)(H_2O)$_2$](ClO_4) (**3**), of an anthracene-appended multifunctional organic scaffold, **Hahpa** (**Hahpa** = 3-((anthracene-10-ylmethyl)(2-hydroxyethyl)amino)propanoic acid), were synthesized and characterized. Synthesis of **1–3** was accomplished by reacting **Hahpa** with zinc(II) precursors such as $ZnCl_2$, $Zn(NO_3)_2{\cdot}6H_2O$ and $Zn(ClO_4)_2{\cdot}6H_2O$, respectively, in the presence of NaOH at room temperature. Compounds **1–3** were characterized by elemental analysis, FTIR, electronic absorption and emission spectroscopy, molar conductivity analysis, and TGA studies. Elemental analysis, molar conductivity analysis, and UV-vis and fluorescence titration results unambiguously confirm the integrity of the compound frameworks. Moreover, the structures of **1–3** were ascertained by density functional theory (DFT) computation using the B3LYP/6-311G level of theory, indicating a distorted square pyramidal geometry around the zinc centers. Furthermore, the anticancer properties of **1–3** were assessed in human cervical cancer (HeLa) cell lines, revealing a significantly high cytotoxicity with IC_{50} values ranging from 1.09 to 2.11 μM. They showed high selectivity between the normal and cancer cells despite this potency. The anticancer activity of **1–3** was possibly due to an increase in cellular reactive oxygen species (ROS), destruction of cell membrane integrity, and DNA damage occurring *via* nuclear condensation. Electronic absorption spectroscopy, ethidium bromide (EB) displacement assay and circular dichroism (CD) spectroscopy confirmed the binding affinity and binding mode of **1–3** with DNA in a dose-dependent manner. All three compounds were also able to modulate the expression of p53 tumour suppressor protein and exhibited antitumorigenic activity, whereas their activity remained unaltered in the normal cell. When a comparative assessment of anticancer properties of **1–3** was made, **1** showed a higher cytotoxicity towards the cancer cells in comparison to **2** and **3**.

Received 25th December 2024,
Accepted 21st January 2025

DOI: 10.1039/d4ma01278j

rsc.li/materials-advances

Introduction

The design and synthesis of therapeutically active new multifunctional organic scaffolds and their metal compounds for cancer treatment are important areas of interdisciplinary research.[1,2] Over the past few decades, significant achievements have been made in this area, including the development of organic, inorganic and composite material-based nanodrugs for preclinical and clinical cancer treatment.[3–6] However, the early-stage diagnosis and effective treatment of cancer are still challenging, specifically due to the multidrug resistance and inadequate availability of cancer-targeting therapeutic drugs.[7,8] In this context, the nanosized antitumor agents have been widely studied owing to their good lesion specificity and improved bioavailability and biodistribution; however they suffer from poor efficacy and serious side effects.[9,10] Hence, there is a demanding need to develop new anticancer drugs to overcome such drawbacks. It is worth mentioning that the success of cisplatin and its derivatives such as oxaliplatin and carboplatin as anticancer drugs has paved the way for discovery of newer and more effective metal-based anticancer drugs.[11] The multifunctional organic scaffold-based metal compounds

[a] *Department of Chemistry, University of Kalyani, Kalyani, Nadia, West Bengal-741235, India. E-mail: mbera2009@klyuniv.ac.in; Fax: +91 33 25828282; Tel: +91 33 25828282x306*

[b] *Cytogenetics and Molecular Biology Lab., Department of Zoology, University of Kalyani, Kalyani, Nadia, West Bengal-741235, India*

† Electronic supplementary information (ESI) available: FTIR, ^{1}H & ^{13}C NMR, and ESI-MS of **Hahpa**; FTIR spectra of **1–3**; UV-vis absorption and fluorescence emission titration spectra, and viscosity measurement concerning the DNA binding studies of **1–3**; Scatchard plots for **1–3**; figures associated with % cytotoxicity of **1–3** in the normal L6 skeletal muscle cell line and % cytotoxicity of the precursor zinc salts in the HeLa cell line; and fluorescence intensity histogram profiles showing the expression of p53 protein and nuclear condensation in **1–3** treated HeLa cells. See DOI: https://doi.org/10.1039/d4ma01278j

have prominent roles in cancer chemotherapy since several metal ions are crucial for numerous biological processes.[12] In particular, several ruthenium-based luminescent compounds are identified as potential theragnostic probes due to their easy synthesis, structural modification and functional tunability.[13,14] However, their poor selectivity and dose-dependent toxicity limit their long-term usage for cancer treatment.[15] Recently, some other ruthenium-based compounds such as NAMI-A, KP1019 and (N)KP1339 have been discovered as potential anticancer agents because of their improved cancer selectivity.[16,17]

Zinc is the second most abundant transition metal in our body and considered as an indispensable element for human physiology. It is very crucial for cell survival, proliferation, and differentiation.[18] Zn(II) ions play an important role as a cofactor of several intracellular enzymes.[19,20] Thus, zinc is required for critical functions in humans such as immunity and reproduction.[21,22] It is also established that cancer is strongly related to zinc deficiency. For example, zinc enhances the immune response and function of white blood cells in cancer patients.[23] Zinc ions can mitigate the cardiotoxicity and hepatotoxicity of anticancer drugs due to its potential to enable Lewis acid activation, nucleophile formation, and fast ligand exchange.[24] However, a very few zinc-based chemotherapeutic drugs are reported to serve as alternatives to platinum-based anticancer drugs.[25,26] It is also believed that the binding of Zn(II) with appropriately designed multifunctional organic scaffolds improves bioavailability and biodistribution and reduces the overall cost of drug formulation while availing the beneficial outcome against cancer. Moreover, the cellular uptake of Zn(II) compounds is supposed to be driven by specific binding to transferrin and human serum albumin so that they can cause less toxicity to healthy cells, while the uptake of other transition metal compounds involves passive diffusion.[27,28] Unfortunately, significantly fewer research investigations into anticancer Zn(II) compounds have been conducted. The present study originates from our ongoing research endeavour that is undertaken to systematically study 3d transition metal-based compounds of carboxylate-incorporated multifunctional organic assemblies.[29–36] In our current research, we have successfully introduced an anthracene backbone as a signalling agent within a multifunctional organic scaffold, thus resulting in the formation of **Hahpa** (**Hahpa** = 3-((anthracene-10-ylmethyl)(2-hydroxyethyl)amino)propanoic acid), with a desired degree of flexibility of the donor atoms for metal binding (Scheme 1). Thorough literature search reveals that the currently available and clinically active anticancer drugs such as doxorubicin, mitoxantrone, and camptothecin contain the anthracene backbone as a significant part of their molecular structures.[37–39] These drugs are believed to function *via* the inhibition of DNA topoisomerases, particularly topoisomerase II. Therefore, motivated by the challenges and our continuing research interest in designing and synthesizing some smart organic scaffolds for exploration of promising biological properties, the main focus of our interest was to develop a family of Zn(II) compounds incorporating the anthracene backbone. In the present article, the design and synthesis, structural and physicochemical characterization, and evaluation of three novel Zn(II) compounds [Zn(ahpa)(Cl)(H_2O)] (**1**), [Zn(ahpa)(NO_3)(H_2O)] (**2**) and [Zn(ahpa)(H_2O)$_2$](ClO_4) (**3**) as promising chemotherapeutic agents against cervical cancer have been explored through well-established scientific evidence.

Results and discussion

Design, synthesis and general characterization of a multifunctional organic scaffold (Hahpa) and its Zn(II) compounds (1–3)

The synthesis of an anthracene-appended new multifunctional organic scaffold, **Hahpa,** is illustrated in Scheme 1. This organic scaffold has one alcohol, one carboxylate and one tertiary amine-based O_2N donor atom as the metal binding sites and one pendant anthracene backbone as the signalling component. **Hahpa** has been characterized by standard analytical and spectroscopic techniques such as elemental analysis,

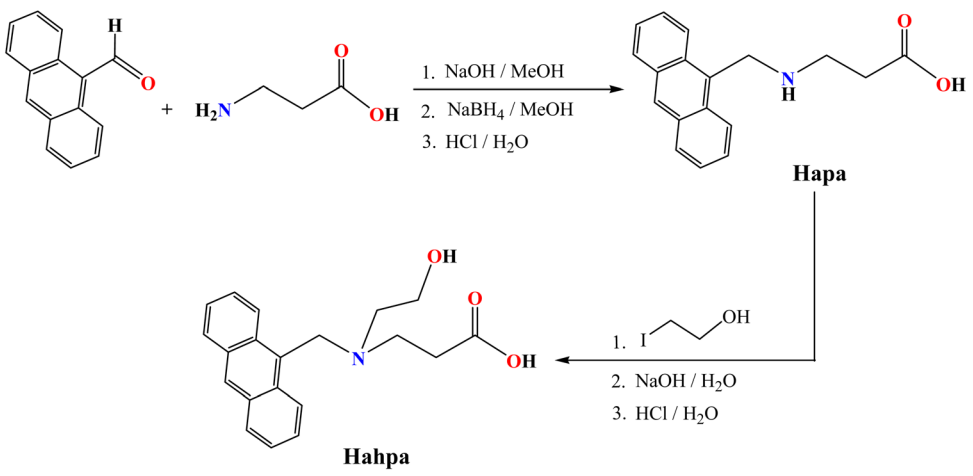

Scheme 1 Synthetic pathway of the multifunctional organic scaffold, **Hahpa**.

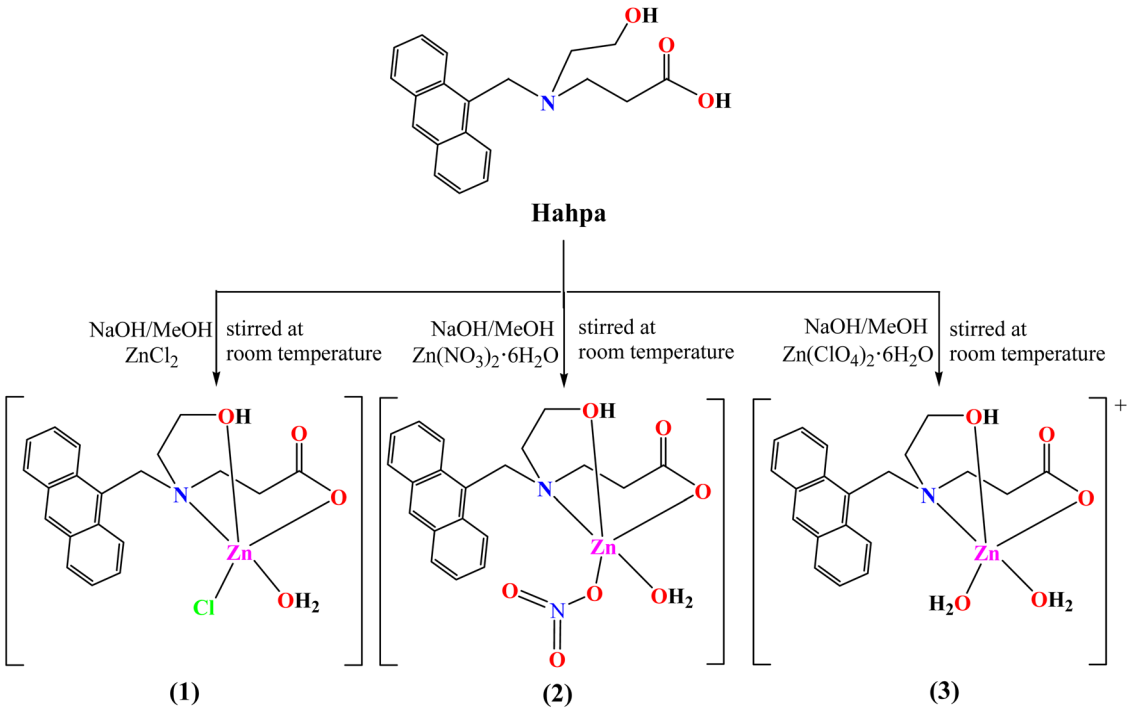

Scheme 2 Synthetic pathway of compounds **1–3**.

FTIR (Fig. S1, ESI†), ^{1}H and ^{13}C NMR (Fig. S2 and S3, ESI†) and ESI-MS (Fig. S4, ESI†). Compounds **1–3** were synthesized in excellent yield (70–80%) by adding a mixture of **Hahpa** and NaOH to the respective Zn(II) salts separately, in methanol solution. A general synthetic protocol of compounds **1–3** is depicted in Scheme 2. Briefly, the room temperature reactions of one equiv. of **Hahpa** with one equiv. of $ZnCl_2$, $Zn(NO_3)_2{\cdot}6H_2O$ and $Zn(ClO_4)_2{\cdot}6H_2O$, separately, in the presence of NaOH in methanol produced compounds $[Zn(ahpa)(Cl)(H_2O)]$ (**1**), $[Zn(ahpa)(NO_3)(H_2O)]$ (**2**) and $[Zn(ahpa)(H_2O)_2](ClO_4)$ (**3**), respectively. Characterization of these compounds was performed by elemental analysis, molar conductance analysis, FTIR, UV-vis and fluorescence spectroscopy, TGA analysis, including molecular structure optimization using density functional theory (DFT) calculations. The DFT calculations provided the metric parameters and geometrical arrangements around the zinc centers in **1–3**. The molar conductance (Λ_M) values of **1**, **2** and **3** measured in DMF solution are 17, 10 and 80 Ω cm^2 mol^{-1}, respectively.

As indicated by these values, compounds **1** and **2** are non-electrolytic formulations, while compound **3** is of 1 : 1 electrolyte-type.[40] The FTIR spectra (Fig. S5–S7, ESI†) of **1–3** showed characteristic asymmetric (ν_{as}) and symmetric (ν_s) stretching bands of the carboxylates: 1570 (ν_{as}) and 1403 cm^{-1} (ν_s) for **1**, 1583 (ν_{as}) and 1384 cm^{-1} (ν_s) for **2**, and 1594 (ν_{as}) and 1407 cm^{-1} (ν_s) for **3**. The relatively higher value of Δ (Δ = $\nu_{as}(COO^-) - \nu_s(COO^-)$) at ~167, 199 and 187 cm^{-1} for **1**, **2** and **3**, respectively strongly suggests the monodentate terminal binding of the carboxylate functionalities.[41] The bands observed between 3424 and 3453 cm^{-1} correspond to the ν(O–H) vibrations of the coordinated H_2O molecules in **1–3**. In addition, the terminal coordination of the NO_3^- group in compound **2** is suggested by the occurrence of sharp bands at 1789 and 1325 cm^{-1}.[42] Verification of an uncoordinated ClO_4^- ion outside the coordination sphere in compound **3** is indicated by a sharp unsplit band at 1090 cm^{-1}.[43]

Photophysical properties: UV-vis absorption and fluorescence titration studies

In order to understand the binding events of the newly designed multifunctional organic scaffold **Hahpa** with Zn(II), the changes in its photophysical properties induced by addition of different Zn(II) salts were studied in solution by employing UV-vis absorption and fluorescence emission titrations. The binding of different Zn(II) salts with **Hahpa** brought about significant changes in both the absorption and emission features of the attached anthracene backbone. These studies also indicated the composition and stability of compounds **1–3** formed upon binding of **Hahpa** with Zn(II).

Fig. 1 illustrates the UV-vis titration spectra of **Hahpa** with different Zn(II) salts in methanol solution. The electronic absorption spectrum of **Hahpa** exhibits intense absorption bands at 385, 365, 347 and 331 nm due to π–π^* transitions of the anthracene backbone.[44] Upon gradual addition of $ZnCl_2$, $Zn(NO_3)_2{\cdot}6H_2O$ and $Zn(ClO_4)_2{\cdot}6H_2O$ separately to a methanol solution of **Hahpa**, the absorption bands at 385, 365, 347 and 331 nm increased progressively, with a significant red shift of the absorption maxima by 2–4 nm in the case of all three Zn(II) salts, indicating that the $(Zn^{2+})/(ahpa)^-$ compounds were formed in solution. The increase in the absorption bands

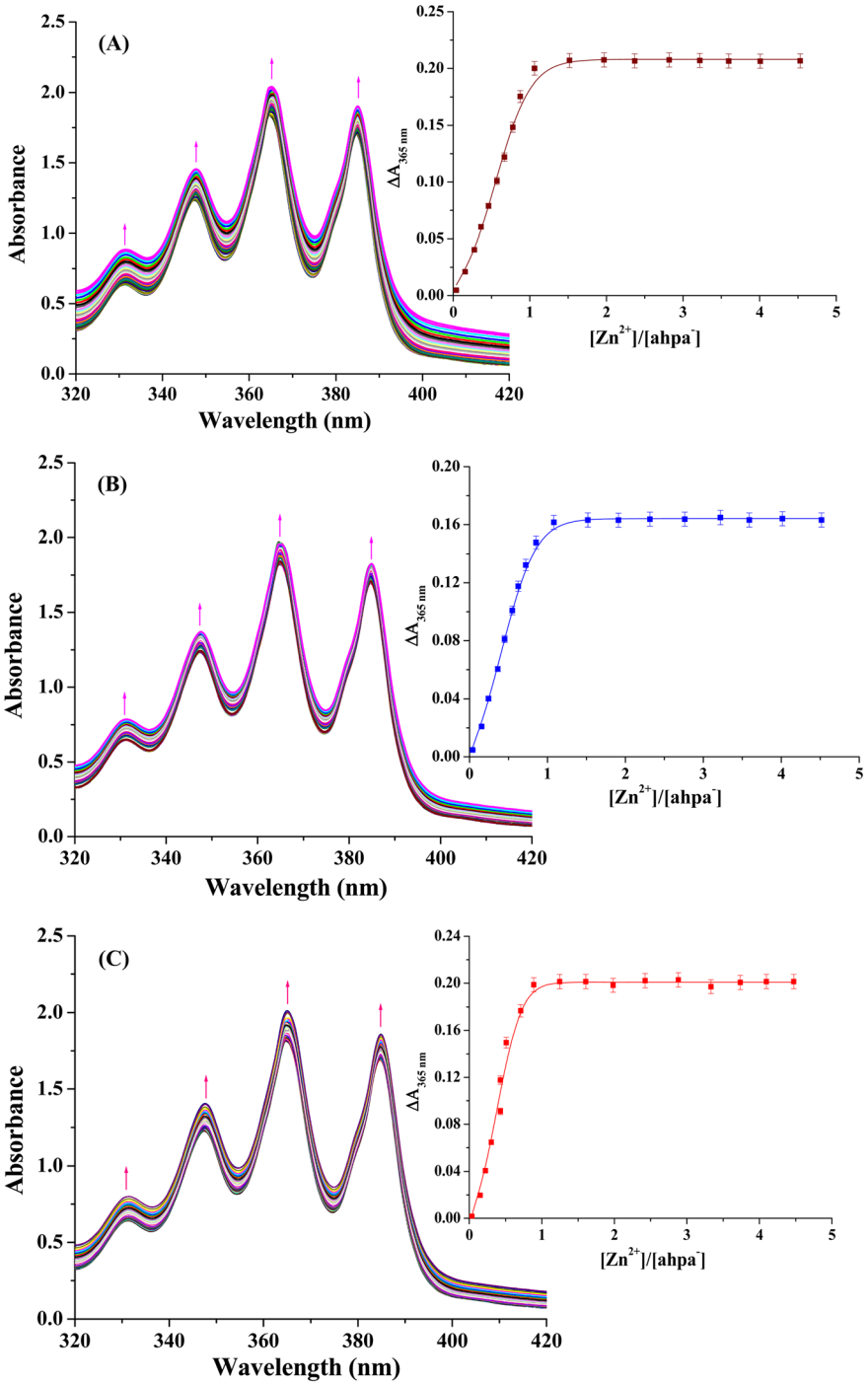

Fig. 1 UV-vis titration spectra of the multifunctional organic scaffold $(ahpa)^-$ (1.013×10^{-4} M) acquired on adding (A) $ZnCl_2$, (B) $Zn(NO_3)_2{\cdot}6H_2O$, and (C) $Zn(ClO_4)_2{\cdot}6H_2O$ in MeOH solution at room temperature; the concentrations of Zn(II) salts were varied from 0 to 4.526×10^{-4} M. (inset) The corresponding titration curves of (A) $ZnCl_2$, (B) $Zn(NO_3)_2{\cdot}6H_2O$, and (C) $Zn(ClO_4)_2{\cdot}6H_2O$ according to the absorption intensity, indicating 1 : 1 stoichiometry for $(Zn^{2+})/(ahpa)^-$ (**1**).

continued up to a molar ratio of 1 : 1 for $(Zn^{2+})/(ahpa)^-$. Fig. 1 insets show the titration profiles for $ZnCl_2$, $Zn(NO_3)_2{\cdot}6H_2O$ and $Zn(ClO_4)_2{\cdot}6H_2O$ confirming the formation of the 1 : 1 $(Zn^{2+})/(ahpa)^-$ bound assemblies in solution. The spectral changes observed upon binding of Zn(II) with the $(ahpa)^-$ scaffold are very similar to the results reported by our research group for the interaction of Zn(II) with anthracene-incorporated μ-bis(tridentate) organic assembly.[36] Addition of increasing concentrations of Zn(II) ions to the $(ahpa)^-$ scaffold induced the red-shift of the absorption bands, which clearly explained the high stability of the as-synthesized Zn(II) compounds (**1–3**). Accordingly, the binding constant (K_b) values were calculated

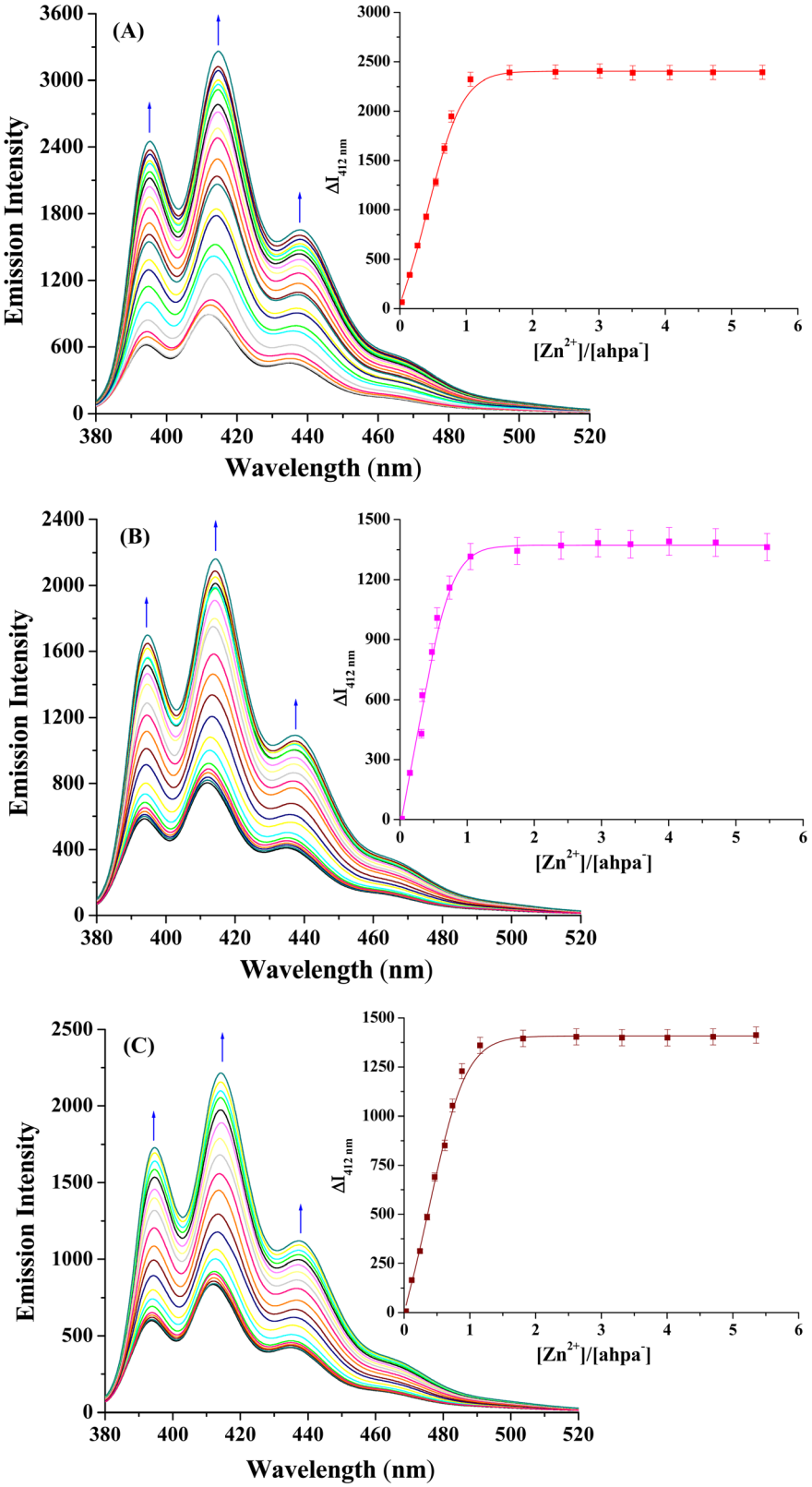

Fig. 2 Fluorescence titration spectra of the multifunctional organic scaffold $(ahpa)^-$ (1.013×10^{-4} M) acquired on adding (A) $ZnCl_2$, (B) $Zn(NO_3)_2{\cdot}6H_2O$, and (C) $Zn(ClO_4)_2{\cdot}6H_2O$ in MeOH solution at room temperature; the concentrations of Zn(II) salts were varied from 0 to 5.480×10^{-4} M. (inset) The corresponding titration curves of (A) $ZnCl_2$, (B) $Zn(NO_3)_2{\cdot}6H_2O$, and (C) $Zn(ClO_4)_2{\cdot}6H_2O$ according to the emission intensity, indicating 1 : 1 stoichiometry for $(Zn^{2+})/(ahpa)^-$ (**1**).

using the UV-vis titration data by applying the method of Rose and Drago.[45] The calculated K_b values of the organic scaffold-bound Zn(II) compounds are $(2.31 \pm 0.14) \times 10^4\ M^{-1}$, $(2.10 \pm 0.17) \times 10^4\ M^{-1}$ and $(3.66 \pm 0.10) \times 10^4\ M^{-1}$ for **1**, **2** and **3**, respectively.

In order to further demonstrate the ability of **Hahpa** to bind with Zn(II), the fluorescence titration experiments of **Hahpa** with different zinc salts were performed in methanol solution. The emission spectrum of **Hahpa**, which was excited at 365 nm, showed strong emission bands at 436, 412 and 394 nm at room temperature in methanol solution. These emission bands are typical for the attached anthracene backbone.[36] The fluorescence titration spectra acquired from the titration of **Hahpa** with increasing concentrations of $ZnCl_2$, $Zn(NO_3)_2{\cdot}6H_2O$ and $Zn(ClO_4)_2{\cdot}6H_2O$ are displayed in Fig. 2. As seen, the gradual addition of the respective Zn(II) salt to the methanol solution of **Hahpa** causes significant enhancement of its fluorescence intensities, with a considerable red shift of the emission maxima by 2–3 nm. The observed fluorescence intensity was virtually proportional to the concentration of the Zn(II) salt. The saturation behavior of the emission intensity after addition of 1 equiv. of Zn(II) indicates that the 1 : 1 $(Zn^{2+})/(ahpa)^-$ bound assemblies (**1–3**) are formed in solution (Fig. 2 insets). The chelation promoted fluorescence-on can be justified by considering that the Zn(II) ions with completely filled d-orbitals are known to increase the fluorescence intensity *via* either the photo-induced electron transfer or energy transfer mechanism.[46] The binding constant (K_b) values of $(Zn^{2+})/(ahpa)^-$ assemblies calculated from the fluorescence titration data are found to be $(5.27 \pm 0.20) \times 10^3\ M^{-1}$, $(4.86 \pm 0.28) \times 10^3\ M^{-1}$ and $(6.38 \pm 0.16) \times 10^3\ M^{-1}$ for **1**, **2** and **3**, respectively. The fluorescence titration outcomes suggest that the multi-functional organic scaffold **Hahpa** forms 1 : 1 compounds with Zn(II) ions in solution.

Thermal studies

The thermogravimetric analysis (TGA) of compounds **1–3** was performed to understand their thermal behavior. The TGA curves of **1–3** are displayed in Fig. 3. The first decomposition step of **1** shows a mass loss between 43 and 74 °C due to the removal of a coordinated water molecule. The mass loss detected in this step is 3.84% (calcd 4.08%). The second decomposition step observed between 308 and 400 °C is due to the release of one CO_2 and half Cl_2 gases corresponding to a mass loss of 18.01% (calcd 18.05%). The decomposition of the overall metal–organic framework takes place between 480 and 850 °C. For thermal decomposition of **2**, the first step proceeds between 55 and 97 °C with a mass loss of 4.51% (calcd 3.86%), attributed to the loss of a coordinated water molecule. The second decomposition step that occurred between 270 and 351 °C is attributed to the release of one CO_2 and one NO gas molecules, which corresponds to a mass loss of 15.75% (calcd 15.85%). The third decomposition step that occurred between 477 and 853 °C is associated with the disintegration of the overall metal–organic framework. Similarly, compound **3** shows a three-step thermal decomposition reaction. The first

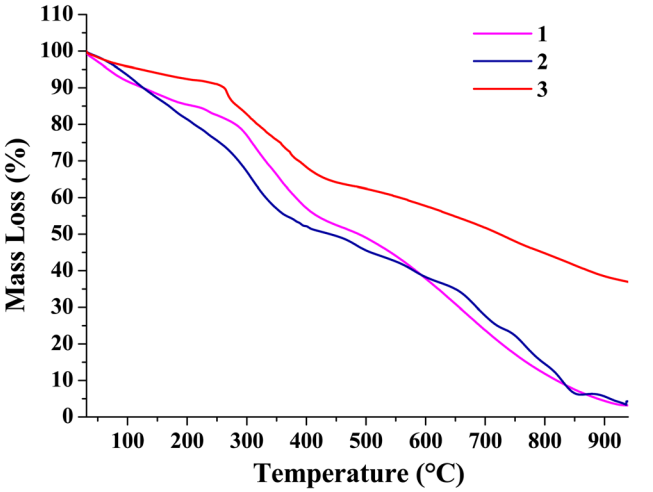

Fig. 3 TGA curves of [Zn(ahpa)(Cl)(H_2O)] (**1**), [Zn(ahpa)(NO_3)(H_2O)] (**2**) and [Zn(ahpa)(H_2O)$_2$](ClO_4) (**3**) under an inert atmosphere of nitrogen gas at a heating rate of ~12 °C min^{-1}.

decomposition step happens between 35 and 195 °C with a mass loss of 7.89% (calcd 8.52%), corresponding to the removal of two coordinated water molecules. The second decomposition step observed between 264 and 398 °C with a mass loss of 17.66% (calcd 17.97%) is attributed to the removal of one CO_2 and one O_2 gas molecules. The third and final step takes place between 460 and 878 °C showing the decomposition of the overall metal–organic framework. ZnO is formed as the most possible residual end product for all three complexes.[47] A careful literature study reveals that analogous thermal features are observed for carboxylate, chloride, nitrate and perchlorate-based metal compounds that release CO_2, Cl_2, NO and O_2 gases, respectively.[48–51]

Structural optimization by density functional theory (DFT) calculations

The structures of all three Zn(II) compounds were optimized by density functional theory (DFT) calculations in order to obtain insight into their molecular arrangements, along with the metric parameters and geometry around the metal centers. Tables 1–3 summarize the selected bond distances and angles of **1–3**. Views of their optimized structures are depicted in Fig. 4. The structures of **1–3** are in good agreement with the

Table 1 Selected bond distances (Å) and angles (deg) for [Zn(ahpa)(Cl)(H_2O)] (**1**) acquired from the DFT-B3LYP/6-311G level of theory

Bond distances [Å]		Bond angles [deg]	
Zn(45)–O(1)	1.9304	O(1)–Zn(45)–O(2)	149.77
Zn(45)–O(2)	1.9288	O(1)–Zn(45)–O(4)	95.88
Zn(45)–O(4)	1.9088	O(1)–Zn(45)–N(7)	83.51
Zn(45)–N(7)	1.9564	O(1)–Zn(45)–Cl(49)	104.95
Zn(45)–Cl(49)	2.2398	O(2)–Zn(45)–O(4)	78.59
		O(2)–Zn(45)–N(7)	89.30
		O(2)–Zn(45)–Cl(49)	105.22
		O(4)–Zn(45)–N(7)	154.85
		O(4)–Zn(45)–Cl(49)	104.03
		N(7)–Zn(45)–Cl(49)	100.37

Table 2 Selected bond distances (Å) and angles (deg) of [Zn(ahpa)-(NO_3)(H_2O)] (**2**) acquired at the DFT-B3LYP/6-311G level of theory

Bond distances [Å]		Bond angles [deg]	
Zn(52)–O(1)	1.9348	O(1)–Zn(52)–O(2)	150.75
Zn(52)–O(2)	1.9251	O(1)–Zn(52)–O(4)	95.91
Zn(52)–O(4)	1.9105	O(1)–Zn(52)–O(46)	104.16
Zn(52)–O(46)	1.9091	O(1)–Zn(52)–N(7)	83.16
Zn(52)–N(7)	1.9580	O(2)–Zn(52)–O(4)	78.68
		O(2)-Zn(52)–O(46)	104.99
		O(2)–Zn(52)–N(7)	89.31
		O(4)–Zn(52)–N(7)	153.69
		O(4)–Zn(52)–O(46)	105.43
		N(7)–Zn(52)–O(46)	100.24

Table 3 Selected bond distances (Å) and angles (deg) of [Zn(ahpa)-(H_2O)$_2$](ClO_4) (**3**) acquired at the DFT-B3LYP/6-311G level of theory

Bond distances [Å]		Bond angles [deg]	
Zn(45)–O(1)	1.9449	O(1)–Zn(45)–O(2)	163.39
Zn(45)–O(2)	1.9184	O(1)–Zn(45)–O(4)	107.04
Zn(45)–O(4)	1.9099	O(1)–Zn(45)–O(49)	65.78
Zn(45)–O(49)	1.9101	O(1)–Zn(45)–N(7)	79.50
Zn(45)–N(7)	2.0180	O(2)–Zn(45)-O(4)	79.59
		O(2)–Zn(45)–O(49)	105.57
		O(2)–Zn(45)–N(7)	90.48
		O(4)–Zn(45)–N(7)	164.24
		O(4)–Zn(45)–O(49)	63.90
		N(7)–Zn(45)–O(49)	107.88

spectroscopic and analytical data. As shown in Fig. 4, the zinc centers lie in a distorted square pyramidal geometry, as indicated by the values of the Addison parameter, τ (Zn45, 0.085 in **1**; Zn52, 0.049 in **2**; and Zn45, 0.014 in **3**).[52] On the other hand, the square pyramidal geometry around Zn45 in **1** is defined by one nitrogen and two oxygen donor groups (N7, O1 and O2) of the $(ahpa)^-$ scaffold, one oxygen donor from a monodentate water molecule (O4) and an auxiliary chloride ligand (Cl49); the square pyramidal geometry around Zn52 in **2** is defined by one nitrogen and two oxygen donor groups (N7, O1 and O2) of the $(ahpa)^-$ scaffold, and two oxygen donor groups from a monodentate water molecule (O4) and an auxiliary nitrate ligand (O46). In contrast, the square pyramidal geometry around Zn45 in **3** is defined by one nitrogen and two oxygen donor groups (N7, O1 and O2) of the $(ahpa)^-$ scaffold, and two oxygen donor groups from two monodentate water molecules (O4 and O49). The zinc center deviates from the respective square plane by 0.455, 0.458 and 0.234 Å in **1**, **2** and **3**, respectively. The Zn–N and Zn–O bond distances range from 1.9088 to 2.0180 Å (Tables 1–3), which are comparable to the analogous five-coordinate zinc(II) complexes.[53,54] The five- and six-membered chelate rings are markedly non-planar with the bite angles of O(1)–Zn(45)–N(7) = 83.51 and O(2)–Zn(45)–N(7) = 89.30° in **1**; O(1)–Zn(52)–N(7) = 83.16 and O(2)–Zn(52)–N(7) = 89.31° in **2**; O(1)–Zn(45)–N(7) = 79.50 and O(2)–Zn(45)–N(7) = 90.48° in **3**. The zinc centers in **1–3** are linked to the planar anthracene backbone by the $-CH_2-N<$ linker, showing a virtually perpendicular orientation to each other. Careful structural analysis also disclosed that the distances between the Zn(II) ions and the centroid of anthracene rings are 3.903, 3.936 and 3.959 Å in **1**, **2** and **3**, respectively, suggesting a weak intramolecular cation$\cdots\pi$ interaction.[55]

Anticancer properties: quantification of % cytotoxicity

In order to examine the anticancer properties of the Zn(II) compounds, the *in vitro* cytotoxicity of **1–3** was determined first by a trypan blue dye exclusion method using the human cervical cancer (HeLa) cells as they are the most commonly used model human cancer cell lines for the investigation of chemotherapy. The proliferation of HeLa cells treated with **1–3** appeared to be reduced significantly after 24 h of treatment (Fig. 5). The % cytotoxicity was markedly higher in all three compound-treated groups when compared to the control ($^{***}p < 0.001$ *vs.* control). The IC_{50} values were calculated and found to be 1.09 μM for **1**, 1.54 μM for **2**, and 2.11 μM for **3**. Furthermore, these compounds when checked in the normal L6 skeletal muscle cell line did not show any significant change in % cell viability as compared to untreated normal cells (Fig. S8, ESI†). A comparison of these results indicated that **1** is much more effective in reducing cell proliferation, thus resulting in diminished cancer cell growth compared to **2** and **3**. Moreover, the treatment of HeLa cells with precursor zinc salts used in the present study resulted in a very insignificant change in % cytotoxicity (Fig. S9, ESI†).

Studies of cell morphology and cell membrane integrity

The surface morphology of HeLa cells was analyzed by phase contrast and scanning electron microscopy studies. Both the phase contrast and scanning electron microscopic images (Fig. 6 and 7) showed that compounds **1–3** treated groups contained a significant amount of dead HeLa cells, which is in good agreement with the results obtained from the assessment of % cytotoxicity. Critical analysis of these microscopic images revealed the following observations for treatments using compounds **1–3**: (i) the compound **1**-treated group showed the highest number of apoptotic cells (Fig. 6C and 7C), (ii) the compound **2**-treated group showed the cells that acquired an ovoid morphology due to the loss of cellular matrix adherence and an increased number of membrane perforations (Fig. 6D and 7D), (iii) the compound **3**-treated group also showed numerous apoptotic cells; however, in some cases, the cells were completely devoured and cellular remnants were left (Fig. 6E and 7E). When analyzed concertedly, the formation of beaded apoptopodia and other apoptotic bodies, membrane blebbing, membrane disruption and a large number of plasma membrane perforations were observed, indicating the detrimental effects of the Zn(II) compounds that imposed cellular death in the cancer cells.

Monitoring the production of intracellular reactive oxygen species (ROS)

Reactive oxygen species (ROS) play a significant role in controlling the cell proliferation and apoptosis, and hence the mechanistic action of cell death. Extreme and uncontrolled production of ROS leads to oxidative stress, thus accelerating

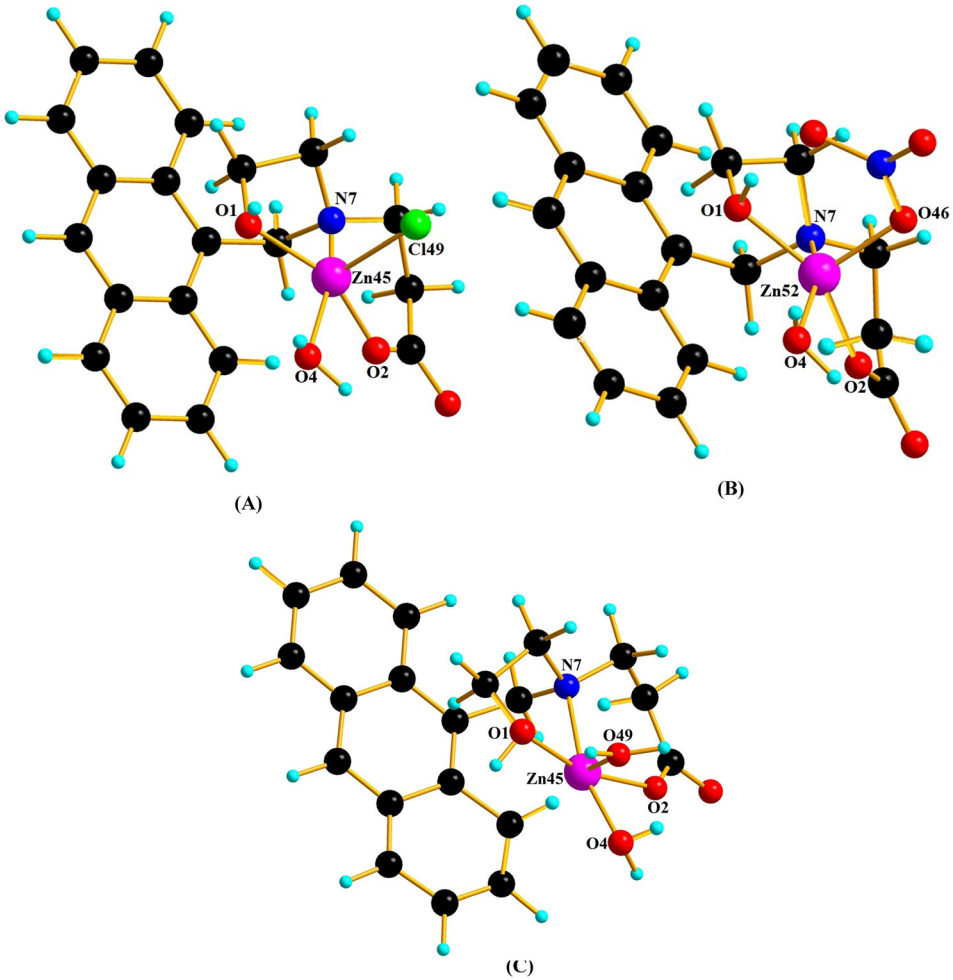

Fig. 4 Geometric and electronic structures of (A) [Zn(ahpa)(Cl)(H_2O)] (**1**); (B) [Zn(ahpa)(NO_3)(H_2O)] (**2**); and (C) [Zn(ahpa)(H_2O)$_2$](ClO_4) (**3**) calculated at the DFT-B3LYP/6-311G level of theory. Color code: Zn, pink; N, blue; O, red; C, black; H, light blue.

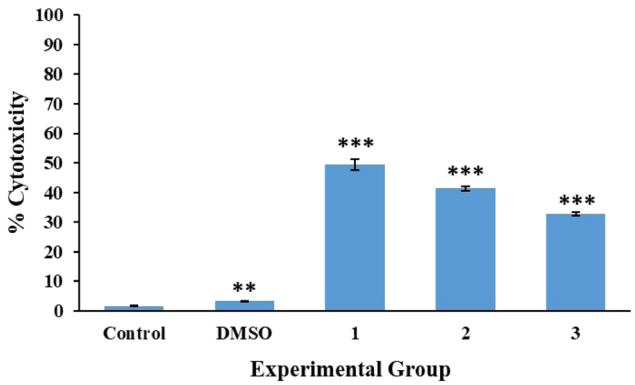

Fig. 5 Graph showing the % cytotoxicity for each experimental group. $^{**}p < 0.01$ *vs.* control; $^{***}p < 0.001$ *vs.* control.

the damage of intracellular components. In fact, due to the abnormal cellular functions, the cancer cells remain under amplified oxidative stress. The H_2DCFDA (H_2DCFDA = 2′,7′-dichlorodihydrofluorescein diacetate) assay revealed that the HeLa cells treated with compounds **1–3** showed significant ROS production after 24 h (Fig. 8). At a glance, the produced ROS break down the two acetate linkages of non-fluorescent H_2DCFDA to yield green fluorescence-based DCF.[56] On the other hand, **1** showed an ∼25% increase in ROS production compared to the control, which was the highest among the three compounds, followed by **2** and **3** with ∼15% and ∼3% increase in ROS production, respectively (Fig. 8). The intensity profiles of ROS mediated by all three Zn(II) compounds suggest their roles in ROS generation, which is followed by cellular apoptosis.

DNA binding studies and UV-vis spectroscopy

Electronic absorption spectroscopy was employed for investigating the binding interactions of compounds **1–3** with DNA. The interactions between compounds **1–3** and CT-DNA were followed by spectral changes arising in the range of 320–400 nm. Fig. S10–S12 of the ESI† depict the UV-vis spectra obtained upon titration of a fixed concentration of **1–3** with increasing concentrations of CT-DNA. The spectra showed the occurrence of ligand-based π–π* transition bands showing a significant hypochromism with a blue shift of 2–3 nm. It is

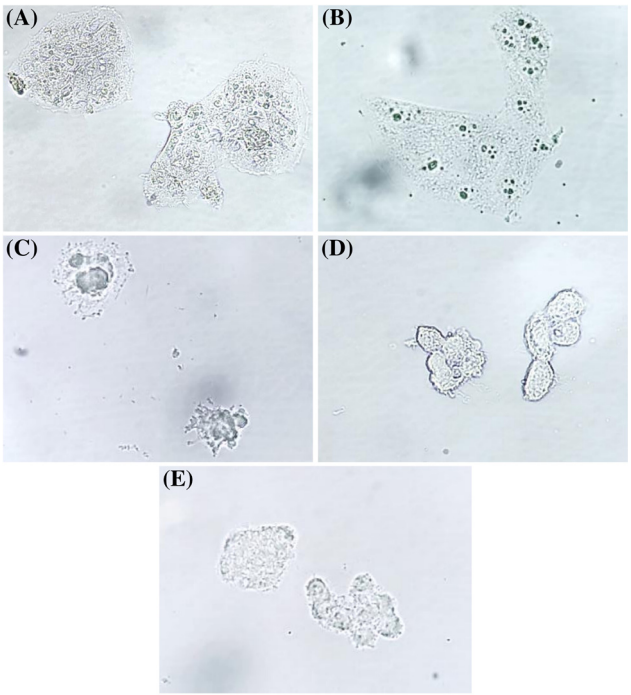

Fig. 6 Phase contrast light microscopic images showing cellular morphology in different experimental groups. (A) control, (B) DMSO, (C) **1**, (D) **2**, and (E) **3**.

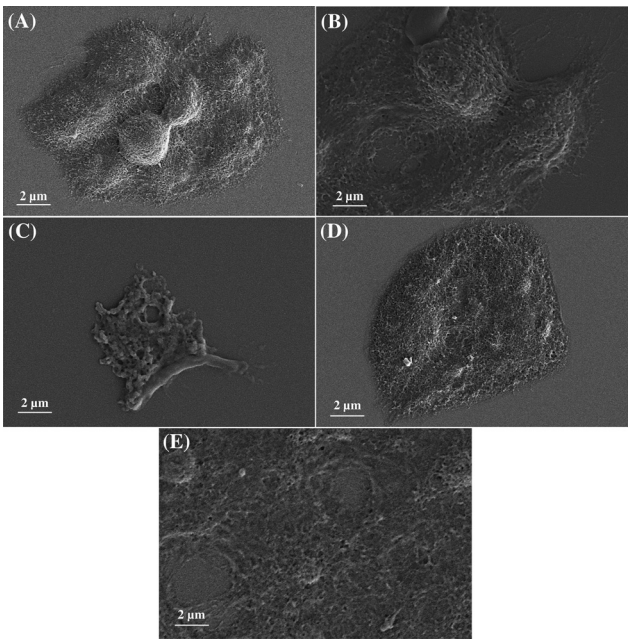

Fig. 7 Scanning electron microscopic (SEM) images showing cellular morphology in different experimental groups. (A) control, (B) DMSO, (C) **1**, (D) **2**, and (E) **3**.

pertinent to mention that the extent of hypochromism is directly proportional to the strength of DNA interaction. A strong stacking interaction between the aromatic chromophore of **1–3** and the adjacent base pairs of CT-DNA resulted in the

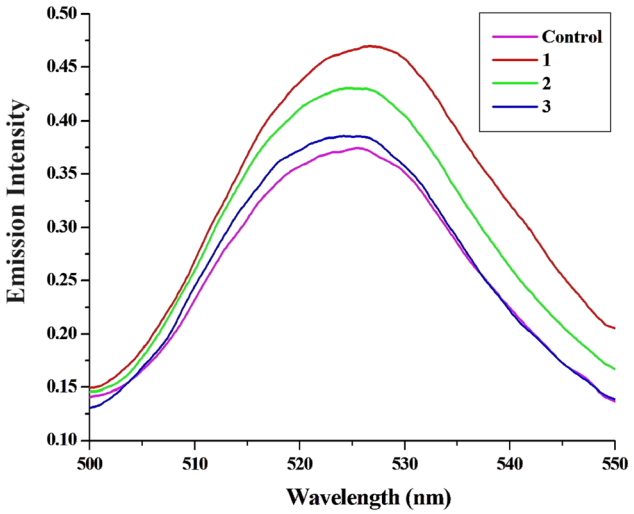

Fig. 8 Spectrofluorometric studies of ROS production in different experimental groups using the H_2DCFDA dye (λ_{exi} = 485 nm; λ_{emi} = 527 nm) and compared against the control.

reduction of transition probability and hence hypochromism.[57] Significant hypochromism and blue shift in the UV-vis titration spectra of **1–3** indicated their interactions with CT-DNA *via* partial intercalation.[58] The following equation (eqn (1)) was used to determine the DNA binding constant (K_b) values:

$$[DNA]/(\varepsilon_a - \varepsilon_f) = [DNA]/(\varepsilon_b - \varepsilon_f) + 1/K_b\,(\varepsilon_b - \varepsilon_f) \quad (1)$$

where [DNA] = concentration of CT-DNA, ε_a = ratio of the absorbance/[compound], ε_f = extinction coefficient of the free metal compound, and ε_b = extinction coefficient of the metal compound present in the completely bound form. The K_b values were calculated to be $(5.07 \pm 0.23) \times 10^4\ M^{-1}$, $(2.62 \pm 0.19) \times 10^4\ M^{-1}$ and $(1.83 \pm 0.15) \times 10^4\ M^{-1}$ for **1**, **2** and **3**, respectively (Fig. S10–S12 insets, ESI†). A comparative analysis of these binding constant values of the studied Zn(II) compounds revealed the order of their binding affinity towards DNA as **1** > **2** > **3**.

DNA binding studies and fluorescence spectroscopy

The binding interactions of compounds **1–3** with DNA were further studied by carrying out ethidium bromide (EB) displacement assay. The emission intensity of free EB is relatively low, but the intensity is significantly enhanced by stacking interaction between the adjacent DNA base pairs. So, the competitive DNA binding experiments of **1–3** were performed by monitoring the changes in the emission intensity of EB bound to CT-DNA as a function of the complex concentration to obtain insight into the binding interactions of the Zn(II) compounds with DNA *via* intercalation.[59] Fig. S13–S15 of the ESI† display the emission spectra of EB bound to CT-DNA acquired upon titration of a fixed concentration of EB/DNA adduct with increasing concentrations of **1–3** separately. The emission intensity of the EB/DNA adduct reduced substantially because of the competition by the corresponding Zn(II) compound in the EB intercalated sites. In the emission titration spectra

(Fig. S13–S15, ESI†), the observed hypochromic shift at ~598 nm indicated that EB was partially replaced by the EB/DNA adduct by the Zn(II) compounds *via* the intercalative interactions. Furthermore, the emission spectra of the Zn(II) compound–DNA adduct also revealed that the emission intensities were reduced by 77%, 75% and 73% for **1**, **2** and **3**, respectively. The DNA binding constant (K_b) values were evaluated using the Scatchard equation (eqn (2))[60,61] as described below:

$$\log[(I_0 - I)/I] = \log[K_b] + n\log[Q] \quad (2)$$

where n = the number of binding sites, I_0 = fluorescence intensity in the absence of the quencher, and I = fluorescence intensity in the presence of the quencher. Therefore, the K_b values obtained from the plots of $\log[(I_0 - I)/I]$ *vs.* $\log[Q]$ (Fig. S16–S18, ESI†) were found to be $(8.58 \pm 0.22) \times 10^3$ M^{-1}, $(5.14 \pm 0.21) \times 10^3$ M^{-1} and $(3.87 \pm 0.19) \times 10^3$ M^{-1} for **1**, **2** and **3**, respectively. These binding constant values suggest the order of the binding strength of the Zn(II) compounds as **1** > **2** > **3**, which agrees well with the observation made in the UV-vis spectral studies.

DNA binding studies and viscosity measurement

In order to explore the mode of binding interactions of **1–3** with DNA, viscosity measurement was performed using the solutions of CT-DNA incubated with the Zn(II) compounds individually. It is well known that intercalative DNA binding would cause an elongation of DNA by increasing the separation of DNA base pairs, leading to an enhancement of viscosity. On the other hand, DNA may bend or twist due to partial or non-classical intercalation of the compound, which would reduce its effective length and viscosity simultaneously. Thus, the relative specific viscosity (η/η_0) of DNA reveals an increase in contour length associated with the separation of DNA base pairs caused by intercalation. Fig. S19 of the ESI† shows the increase in the relative specific viscosity of DNA when **1–3** are added into CT-DNA solution separately. Hence, these results clearly suggest that **1–3** bind to DNA *via* intercalation, which is in accordance with the absorption and fluorescence spectral studies. The ability of the compounds to increase the viscosity of DNA follows the order **1** > **2** > **3**.

DNA binding studies and circular dichroism (CD) spectroscopy

Binding of a small molecule with the right-handed B-form of DNA leads to the change in molar ellipticity, when analysed by circular dichroism (CD) spectroscopy. In the CD spectrum of CT-DNA, the positive band at 275 nm corresponds to base stacking, and the negative band at 245 nm corresponds to helicity, which are the typical characteristics of the right-handed B-form of DNA.[62] Thus, the mode of DNA binding with compounds **1–3** was ascertained by comparing the changes in the positive and negative bands upon addition of the respective Zn(II) compound at different concentrations (Fig. 9). The decrease in the amplitude of the positive CD bands in the range of 275–290 nm accompanied by a minor red-shift corresponded to the change in base stacking interactions of DNA in a concentration-dependent manner for **1–3**.[63] On the other hand, the negative CD bands in the range of 235–250 nm showed a decrease of molar ellipticity in a concentration-dependent manner, with a minor blue-shift, indicating the destabilisation of the right-handed DNA structure.[64] However,

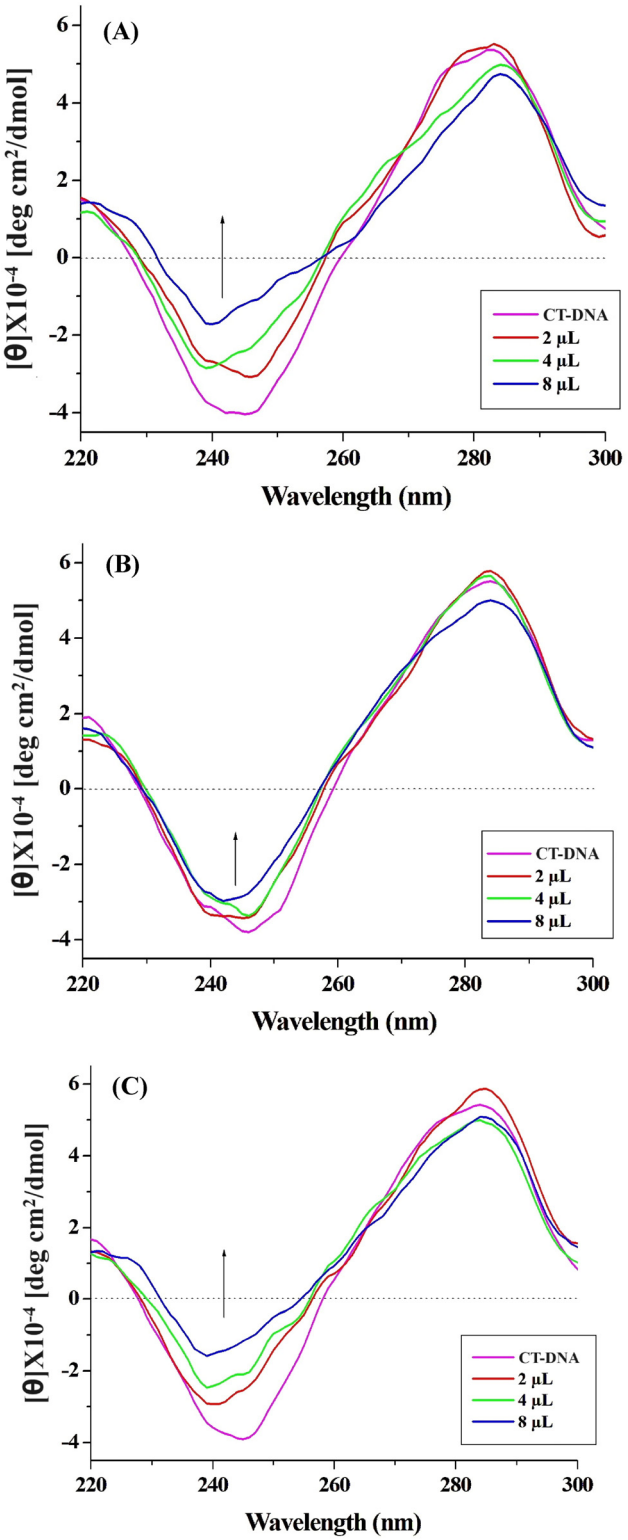

Fig. 9 Circular dichroism (CD) spectra of (A) **1**, (B) **2**, and (C) **3** with CT-DNA showing changes in molar ellipticity in a dose-dependent manner.

a comparison of the CD spectral results specified that compound **1** exhibited the highest change in molar ellipticity in both the positive and negative bands, while compound **2** exhibited the lowest change in molar ellipticity. Additionally, for compound **3**, the negative band showed a significant change in molar ellipticity, which might indicate the dehydration of the B form of DNA and a transition from B to A form.

Studies of p53 protein expression and nuclear condensation

It has been established that p53 is a tumor suppressor gene whose mutation occurs in >50% of tumor cells.[65] Thus, the potential of this tumor protein (p53) has become a prominent research topic in cancer treatment.[66] The immunofluorescence study revealed that all three Zn(II) compounds were found to be capable of inducing the expression of p53 protein in the treated HeLa cells (Fig. 10). The activated p53 protein promotes the cell cycle arrest, thus allowing apoptosis to stop the propagation of cancer cells. As observed from the fluorescence intensity histogram (Fig. 11), compound **1** showed the highest expression of p53 protein, followed by compounds **2** and **3**.

Furthermore, the HeLa cells of experimental and control sets were stained with DAPI (DAPI = 4′,6-diamidino-2-phenylindole) and monitored under a confocal microscope. The microscopic images (Fig. 10) showed that the nuclear morphology became substantially condensed for all three Zn(II) compound-treated cells as indicated by the red arrows, in comparison to the untreated control sets. Generally, apoptosis is strongly believed to be associated with the modification of the structure, function and stability of DNA.[67] The results obtained in the present study supported this observation because one of the advanced steps in apoptosis is DNA damage

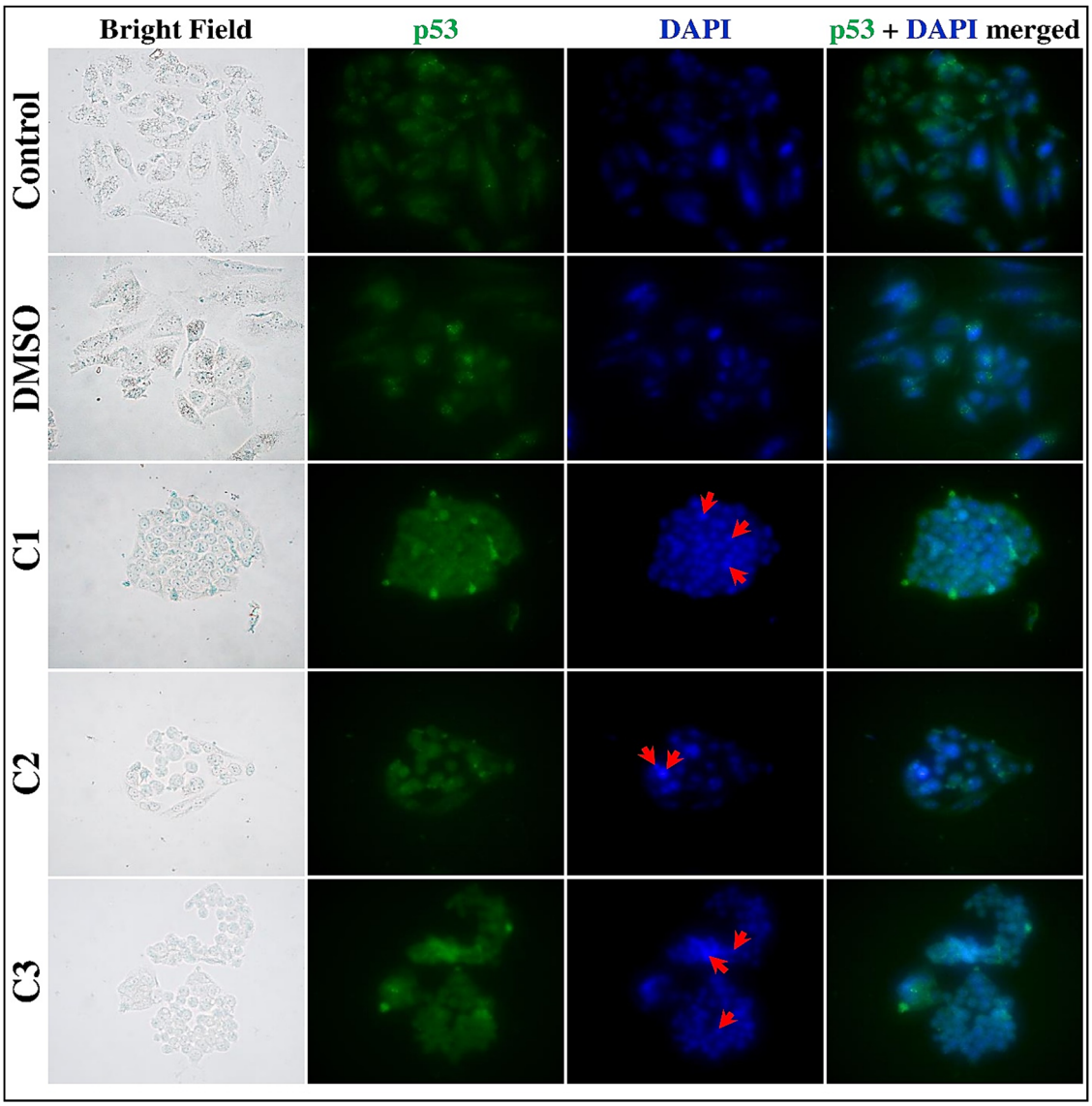

Fig. 10 Immunofluorescence study of p53 protein expression and nuclear condensation using DAPI staining in **1** (C1), **2** (C2), and **3** (C3) treated HeLa cells in comparison to the control group. The red arrows indicate the condensed nuclei.

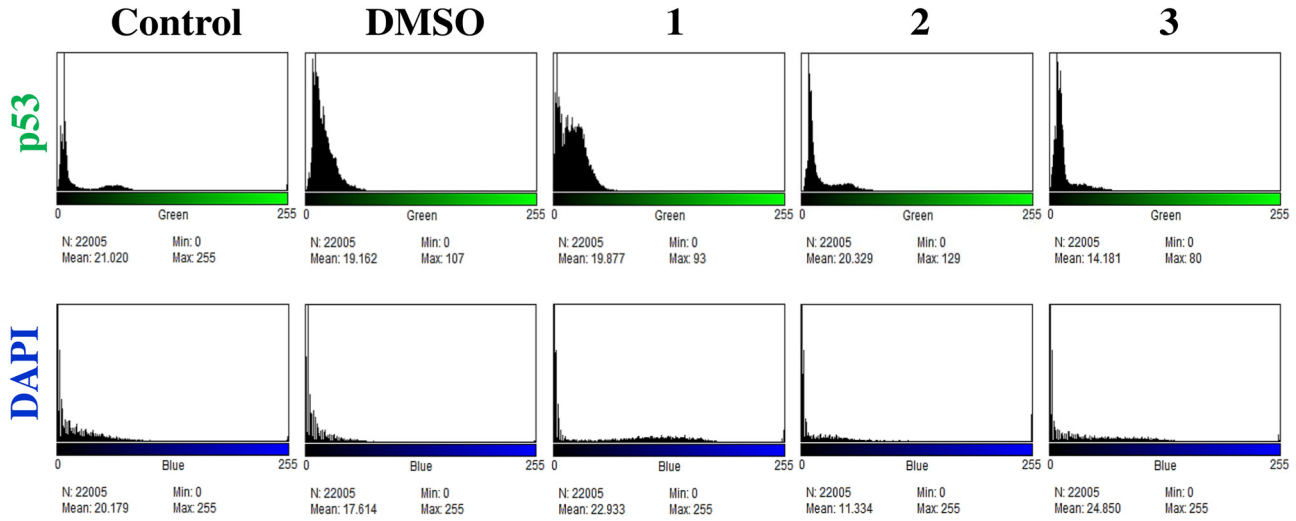

Fig. 11 Histogram profiles of the fluorescence intensities of the p53 protein expression level and DAPI stained nucleus in HeLa cells in different experimental groups.

that results from the nuclear condensation during the apoptotic cell death.[68]

Comparative study of anticancer properties of the Zn(II) compounds (1–3)

The relevance of Zn(II) compounds in biological systems is definitely related to their unique chemical features such as (a) Zn(II) is redox inactive, (b) it is a strong Lewis acid, (c) it has a d^{10} electronic configuration, and hence diamagnetic, (d) it can adopt a varied coordination geometry, and (e) it is prone to a fast exchange of ancillary ligands. The electron affinity of zinc resembles that of nickel or copper, but the lack of redox activity of Zn(II) eliminates any possibility of free radical reactions and makes it vital for the body's antioxidant protection system. On the other hand, literature review also reveals that incorporation of an anthracene backbone within a multifunctional organic scaffold leads to enhanced anticancer activities of their metal compounds due to the increased lipophilic and intercalating properties, which in succession result in their higher cellular uptake.[69] It is well established that increased lipophilicity and intercalating properties of several chelating compounds stimulate the antiproliferative activity.[70] Our results demonstrated that all three Zn(II) compounds exhibited significant anticancer properties when examined in human cervical cancer (HeLa) cell lines. However, among them, **1** showed the highest tumor cell proliferation inhibitory action and consequently anticancer activity. Particularly, while comparing with **2** and **3**, compound **1** was found to exhibit (i) the topmost ROS generation, (ii) highest DNA binding affinity, and (iii) maximum p53 protein expression and nuclear condensation, followed by cellular apoptosis. It is noteworthy to mention that the stimulation of apoptosis in malignant cells is the most preferred mechanism for the treatment of different types of cancers.[71] The results achieved in the present investigation may be attributed to the increased lipophilicity of Zn(II) compounds **1–3**, thereby enhancing their ability to cross the cell membrane. However, it is believed that the chloride-bound metal compounds show superior anticancer properties in comparison to nitro- and aqua-bound metal compounds.[72] Thus, **1** contains a Zn(II)-bound chloride ligand that leaves the coordination sphere easily as a result of the intracellular activation process. Comparing the experimentally obtained IC_{50} values (IC_{50} = 1.09–2.11 μM) with those reported for some analogous Zn(II) compounds, it can be emphasized that there are many reports on the Zn(II) compounds showing lower activity with IC_{50} values of >2.50 μM[73–75] or higher activity with IC_{50} values of <2.50 μM.[76,77] Nevertheless, from these results, very little can be said about the molecular mechanism by which Zn(II) compounds **1–3** elicited their anticancer activity on human cervical cancer (HeLa) cells. Based on these *in vitro* studies, detailed experiments on animals might provide insight into the biological activity of these compounds in tumor-bearing hosts and will help to build clinically relevant information for developing potential anticancer drugs.

Conclusion

In conclusion, the successful design and synthesis, physicochemical and spectroscopic characterization, and assessment of anticancer potential of a novel class of three Zn(II) compounds (**1–3**) of an anthracene-appended multifunctional organic scaffold bearing amine, alcohol and carboxylate functionalities have been described. Different analytical and spectroscopic techniques have been employed to establish the compositions of the compounds in solid and solution states. UV-vis absorption and fluorescence emission titration spectra confirm the 1 : 1 binding model between the $(ahpa)^-$ scaffold and Zn(II) ion in solution. The structures of **1–3** were optimized and ascertained by density functional theory (DFT) computation. On the other hand, **1–3** showed an excellent anticancer efficacy with significant inhibition of % cell viability by inducing apoptotic cell death in HeLa cells; they remained

inefficient in inducing cytotoxicity and apoptosis when administered to normal cells. Furthermore, **1** displayed the highest ROS generation and DNA binding ability and maximum p53 protein expression and nuclear condensation, thus showing a much better anticancer activity in comparison to **2** and **3**. Therefore, from our present exploration, it can be suggested that these novel Zn(II) compounds can be utilized for target-specific chemo-therapeutic drug design for interrupting the molecular mechanism involved in the advancement and propagation of the frightful ailment cancer.

Experimental section

Synthesis of 3-((anthracene-10-ylmethyl)(2-hydroxyethyl)amino)propanoic acid (Hahpa)

A solution of 9-anthracenecarboxaldehyde (2.000 g, 9.69 mmol) in methanol (25 mL) was added dropwise to a solution of β-alanine (0.863 g, 9.69 mmol) and NaOH (0.388 g, 9.69 mmol) in methanol (15 mL) under stirring conditions. After complete addition, the reaction mixture was refluxed for 6 h. Thus, a deep yellow solution of Schiff base was obtained and subsequently it was cooled in an ice-bath. Afterwards, $NaBH_4$ (0.551 g, 14.56 mmol) was added in excess to the cold solution under stirring conditions, resulting in a slight diminishing of the yellow color of the solution. Then, 2 mL of conc. HCl (12 M) was added dropwise to remove excess $NaBH_4$. The solution was then acidified to a pH of ~5 by adding extra conc. HCl (12 M). Next, the solution was filtered and the clear filtrate was rotary evaporated to isolate the precursor ligand 3-[(anthracene-9-ylmethyl)-amino]-propionic acid (**Hapa**) as a yellow crystalline solid. The product was washed with MeOH/H_2O (1 : 4; v/v) and dried in a vacuum desiccator containing anhydrous $CaCl_2$. Yield: 2.165 g (80%). Anal. calc. for $C_{18}H_{17}NO_2$: C, 77.40%; H, 6.13%; N, 5.01%. Found: C, 77.27%; H, 5.99%; N, 5.09%. FTIR (KBr, cm^{-1}): ν = 3386(b), 1624(s), 1449(s), 1385(s), 1344(s), 1288(s), 1262(s), 1218(s), 1160(s), 1053(s), 886(s), 844(s), 784(s), 772(s), 737(s), 702(s), 598(s). ^{1}H NMR (400 MHz, DMSO-d_6, room temperature, δ): 8.80 (s, 1H), 8.52 (d, 2H), 8.20 (d, 2H), 7.71 (t, 2H), 7.62 (t, 2H), 5.27 (s, 2H), 3.65 (s, 2H), 2.86 (t, 1H), 2.76 (t, 1H).

A solution of 2-iodoethanol (1.847 g, 10.74 mmol) in water (15 mL) was added dropwise to a solution of 3-[(anthracene-9-ylmethyl)-amino]-propionic acid (**Hapa**) (3.000 g, 10.74 mmol) and NaOH (0.430 g, 10.74 mmol) in water (40 mL) under stirring conditions. After complete addition, the reaction mixture was refluxed for 6 h. While refluxing, more NaOH (0.143 g, 3.57 mmol) was added to retain the pH of ~11–12. The resulting solution was cooled and acidified with conc. HCl (12 M) up to pH ~5. Subsequently, a light yellow solid product was precipitated. The product was collected by filtration and washed with water and then dried in a vacuum desiccator containing anhydrous $CaCl_2$. The final product was confirmed by elemental analysis, FTIR, ^{1}H and ^{13}C NMR spectroscopy, and mass spectrometry. Yield: 2.613 g (75%). Anal. calc. for $C_{20}H_{21}NO_3$: C, 74.28%; H, 6.55%; N, 4.33%. Found: C, 74.35%; H, 6.67%; N, 4.22%. FTIR (KBr, cm^{-1}): ν = 3427(b), 2925(s), 1709(s), 1621(s), 1588(s), 1449(s), 1387(s), 1259(s), 1181(s), 1051(s), 891(s), 844(s), 785(s), 735(s), 632(s), 600(s), 536(s). ^{1}H NMR (400 MHz, D_2O, room temperature, δ): 8.39 (s, 1H), 8.25 (d, 1H), 8.18 (d, 1H), 7.95-7.98 (m, 2H), 7.41-7.53 (m, 4H), 4.42 (s, 2H), 3.32 (t, 2H), 2.97 (t, 2H), 2.85 (t, 2H), 2.57 (t, 2H). ^{13}C NMR (100 MHz, DMSO-d_6, room temperature, δ): 174.22, 131.40, 131.35, 129.56, 127.44, 126.34, 125.95, 125.50, 124.67, 59.45, 55.13, 50.90, 50.16, 32.16. ESI-MS data: m/z 362.1169 {[**Hahpa** + K]$^+$}, calcd for {[**Hahpa** + K]$^+$} = 362.1159; m/z 453.1700 {[**Hahpa** + 5H_2O + K]$^+$}, calcd for {[**Hahpa** + 5H_2O + K]$^+$} = 453.1720.

Synthesis of Zn(II) compounds (1–3)

Zinc compounds (**1–3**) were prepared by employing the synthetic protocol as described below. For **1**, $ZnCl_2$ (0.105 g, 0.77 mmol) in 10 mL of MeOH was added dropwise to a mixture of **Hahpa** (0.250 g, 0.77 mmol) and NaOH (0.030 g, 0.77 mmol) in 10 mL of MeOH with magnetic stirring for a period of 10 min. For **2**, $Zn(NO_3)_2{\cdot}6H_2O$ (0.229 g, 0.77 mmol) in 10 mL of MeOH was added dropwise to a mixture of **Hahpa** (0.250 g, 0.77 mmol) and NaOH (0.030 g, 0.77 mmol) in 10 mL of MeOH with magnetic stirring for a period of 10 min. Similarly, for **3**, $Zn(ClO_4)_2{\cdot}6H_2O$ (0.287 g, 0.77 mmol) in 10 mL of MeOH was added dropwise to a mixture of **Hahpa** (0.250 g, 0.77 mmol) and NaOH (0.030 g, 0.77 mmol) in 10 mL of MeOH with magnetic stirring for a period of 10 min. The reaction mixture was stirred vigorously for all three reaction sets at ambient temperature for 1 h, resulting in a light yellow solution. The crystalline light yellow compounds were separated gradually upon stirring for 1 h. The compounds were isolated by filtration, washed with water to obtain pure compounds of **1–3**, and dried in a vacuum desiccator containing anhydrous $CaCl_2$.

[Zn(ahpa)(Cl)(H_2O)] (1). Yield: 0.272 g (80%). Anal. calcd for $C_{20}H_{21}NO_4ClZn$: C, 54.57%; H, 4.81%; N, 3.18%; Zn, 14.85; found: C, 54.61; H, 4.67; N, 3.02; Zn, 14.99. FTIR (KBr, cm^{-1}): ν = 3424(b), 1570(s), 1403(s), 1282(s), 1053(s), 887(s), 734(s), 654(s). Molar conductance, Λ_M: (DMF) = 17 Ω^{-1} cm^2 mol^{-1}.

[Zn(ahpa)(NO_3)(H_2O)] (2). Yield: 0.270 g (75%). Anal. calcd for $C_{20}H_{21}N_2O_7Zn$: C, 51.46; H, 4.53; N, 6.00; Zn, 14.01; found: C, 51.59; H, 4.59; N, 6.09; Zn, 13.78. FTIR (KBr, cm^{-1}): ν = 3453(b), 1789(s), 1583(s), 1384(s), 1325(s), 1053(s), 895(s), 836(s), 738(s), 635(s). Molar conductance, Λ_M: (DMF) = 10 Ω^{-1} cm^2 mol^{-1}.

[Zn(ahpa)(H_2O)$_2$](ClO_4) (3). Yield: 0.229 g (70%). Anal. calcd for $C_{20}H_{23}NO_5Zn$: C, 56.82; H, 5.48; N, 3.31; Zn, 15.47; found: C, 56.71; H, 5.51; N, 3.42; Zn, 15.56. FTIR (KBr, cm^{-1}): ν = 3434(b), 1594(s), 1407(s), 1347(s), 1261(s), 1199(s), 1090(s), 963(s), 891(s), 846(s), 737(s), 664(s), 627(s). Molar conductance, Λ_M: (DMF) = 80 Ω^{-1} cm^2 mol^{-1}.

Reagents and solvents

All analytical grade chemicals, reagents and solvents were purchased from commercial sources and used without further purification. 9-Anthracenecarboxaldehyde, β-alanine, 2-iodoethanol and sodium borohydride were purchased from

Sigma-Aldrich, Germany. $ZnCl_2$, $Zn(NO_3)_2{\cdot}6H_2O$, and NaOH were purchased from Merck, India. It is important to mention that $Zn(ClO_4)_2{\cdot}6H_2O$ is potentially explosive, and it should be handled in small quantity with great care. Calf thymus DNA (CT-DNA) was procured from SRL, India. The human cervical cancer (HeLa) cell line was acquired from National Centre for Cell Science (NCCS), Pune, India. The Tris–HCl buffer (pH ~ 7.5) was prepared by using triply distilled and de-ionized water. All the antibiotics, antimycotics and DMEM were obtained from Himedia Laboratories Pvt. Ltd (Mumbai, India), and the foetal bovine serum (FBS) was obtained from Gibco BRL (Grand Island, NY, USA), respectively. The primary antibodies and FITC conjugated secondary antibodies were procured from Santa Cruz Biotechnology (USA) and Sigma-Aldrich (USA), respectively.

General instrumentation methods

The percentage of zinc contents in **1–3** was determined by carrying out a complexometric titration method using Na_2H_2EDTA in aqueous solution, after digesting their crystalline powder samples in a conc. HCl/HNO_3 mixture. The percentages of C, H and N were determined using a PerkinElmer 2400 CHNS/O Series II elemental analyzer. FTIR spectra were recorded on a PerkinElmer L120-000A spectrometer (450–4000 cm^{-1}). The nuclear magnetic resonance spectra were obtained on a Bruker AC 400 MHz NMR spectrometer. UV-vis spectra were performed by employing a Shimadzu UV 1800 (200–900 nm) spectrophotometer. Fluorescence spectra were acquired using a Hitachi F-7000 spectrofluorometer at room temperature. Molar conductivity in solution was measured with a Mettler Toledo Five Easy Plus FEP 30 digital conductivity meter. The TGA studies were performed using NETZSCH STA 449F3 thermal apparatus.

UV-vis absorption spectroscopy

All UV-vis absorption experiments were carried out using a Shimadzu UV 1800 spectrophotometer with a 1 cm quartz cell at room temperature over a wavelength range of 200 to 900 nm. The UV-vis experiments of the multifunctional organic scaffold **Hahpa** with different Zn(II) salts were performed separately in methanol solution by titrating a specified concentration of **Hahpa** (1.013×10^{-4} M) with varying concentrations of the respective Zn(II) salts, such as $ZnCl_2$, $Zn(NO_3)_2{\cdot}6H_2O$ and $Zn(ClO_4)_2{\cdot}6H_2O$, ranging from 0 to 4.526×10^{-4} M. The changes in absorption intensities of the multifunctional organic scaffold $(ahpa)^-$ were documented for the evaluation of stoichiometry and binding constant values of the compounds.

Fluorescence emission spectroscopy

All fluorescence emission experiments were carried out using a Hitachi F-7000 spectrofluorometer with a rectangular quartz cuvette of path length 1 cm at room temperature. The titration experiments of the multifunctional organic scaffold **Hahpa** with different Zn(II) salts were performed separately in methanol solution by titrating a specified concentration of **Hahpa** (1.013×10^{-4} M) with varying concentrations of the respective Zn(II) salts, such as $ZnCl_2$, $Zn(NO_3)_2{\cdot}6H_2O$ and $Zn(ClO_4)_2{\cdot}6H_2O$, ranging from 0 to 5.480×10^{-4} M. The solution was excited at 365 nm for each set of titrations. The changes in emission intensities of the multifunctional organic scaffold $(ahpa)^-$ were documented for the evaluation of stoichiometry and binding constant values of the compounds.

Theoretical calculations

Density functional theory (DFT) calculations[78] regarding the optimization of the structures of all three Zn(II) compounds were performed by employing the B3LYP method[79] and 6-311G basis set.[80,81]

Maintenance of the cell culture and treatment

The cervical cancer cells, HeLa, were cultured and maintained in Dulbecco's Modified Eagle's Medium (DMEM) with 10% FBS and 1% antibiotic solution with antimitotic supplements and kept in the incubator with 5% CO_2 at 37 °C as per the standard procedure.[82] Prior to the *in vitro* treatment, all three compounds were separately dissolved and diluted in PBS buffer (1 : 9; v/v) to make the working solution. The cells were administered with 1 μL per 1 mL of the working solution in fresh cell culture media and incubated for 30 min, after which they were fixed and analyzed for appropriate data. Independent experiments with precursor zinc salts used in the present study were carried out by employing the same method as specified above. The L6 cells (normal cell line), which were used only to check the % of cell viability, were also maintained applying the above-mentioned protocol.

Measurement of % cytotoxicity

The % cytotoxicity in the cervical cancer HeLa cell line and normal L6 skeletal muscle cell line was evaluated by employing the trypan blue dye exclusion method by microscopic quantification of the number of dead cells relative to the total number of cells for each experimental set as per common practice, using the following formula.[83]

$$\%\text{Cytotoxicity} = \frac{\text{Number of dead cells}}{\text{Total number of cells}} \times 100$$

Morphological study of HeLa cells by phase contrast microscopy and scanning electron microscopy

The surface morphology of HeLa cells was studied by phase contrast microscopy and scanning electron microscopy. The cells were seeded on the glass coverslips and were allowed to grow and attain a desirable confluency (70–75%). Following the treatment, the cells were washed with PBS buffer and fixed with 2.5% glutaraldehyde for 2 h.[84] The phase contrast features of the Carl Zeiss Axio Vert-A1 inverted fluorescent microscope were used to capture the images. To dehydrate the cells for the SEM study, the samples were passed through different grades of alcohols and finally placed in a vacuum desiccator overnight. After this, the samples were mounted on aluminium stubs using the double-sided tape and vacuum sputter coated

with gold and palladium. The images were captured using a high-resolution scanning electron microscope (Carl Zeiss EVO LS10) that was set at 20 kV and 10.5 mm working distance.

Quantification of cellular reactive oxygen species (ROS)

The cellular reactive oxygen species (ROS) was quantified by H_2DCFDA following the common practice.[83] An equal number of cells in each group were incubated with 2′,7′-dichlorodihydrofluorescein diacetate (H_2DCFDA) in the dark, and the fluorescence intensity following the conversion of H_2DCFDA to DCF (2′,7′-dichlorodihydrofluorescein) was measured using a fluorescence spectrophotometer (Hitachi F-7100).

DNA binding studies: UV-vis absorption spectroscopy

DNA binding studies of **1–3** were carried out by titrating a specified concentration of each compound (1.010×10^{-4} M) with rising concentrations of CT-DNA (0–8.712×10^{-5} M). The experimental solutions were made in 30 mM Tris–HCl buffer (pH ∼ 7.5) with 5% DMSO. Using electronic absorption spectroscopy, the DNA concentration in solution was determined with a molar extinction coefficient of 13 600 M^{-1} cm^{-1} at 260 nm.[85] The CT-DNA was examined for its purity by monitoring the ratio of the absorbance at 260 nm to that at 280 nm having the value of 1.8–1.9. By adding an equal amount of DNA to both compound and reference solutions, the absorbance of the DNA itself was subtracted.

DNA binding studies: ethidium bromide displacement assay

The DNA binding affinity of **1–3** was further examined by the ethidium bromide (EB) displacement assay. For this, the CT-DNA was incubated first with ethidium bromide ([EB]/[DNA] = 0.1) at 37 °C in the dark for 1/2 h. Then, the solution of the EB/DNA mixture was titrated with rising concentrations of each compound from 0 to 5.762×10^{-3} M after exciting at 510 nm. The emission bands were found at ∼598 nm for **1–3**, respectively.

DNA binding studies: viscosity measurement

The viscosity experiments were carried out using an Ostwald viscometer at room temperature. The viscosity of CT-DNA solution (25×10^{-5} M) was measured in the absence and presence of increasing amounts of the compounds separately in 30 mM Tris–HCl buffer (pH ∼ 7.5) at 25 °C. Flow-time was measured thrice with a digital stopwatch. Viscosity values were presented as $(\eta/\eta_0)^{1/3}$ *versus* [compound]/[DNA],[86] where η is the viscosity of DNA in the presence of the zinc(II) compound and η_0 is the viscosity of DNA in the absence of the zinc(II) compound. Calculation of the relative viscosities was achieved using the relation $\eta = (t - t_0)/t_0$ (t = flow-time of DNA solution in the presence or absence of the compound and t_0 = flow-time of Tris–HCl buffer solution).

DNA binding studies: circular dichroism (CD) spectroscopic study

The CT-DNA was dissolved in tris-buffer saline at a concentration of 1.0 mg mL^{-1}. Different concentrations of each compound were added to the different experimental sets, and the changes in molar ellipticity as a result of the binding interactions were measured by scanning in the wavelength window of 200–400 nm using a Jasco-720 circular dichroism (CD) spectrometer. The path length was 1 cm, the experiments were conducted under a steady nitrogen flush, and the system was maintained at 25 °C.[82]

Immunofluorescence study of p53 protein expression in HeLa cells

The expression of the tumour suppressor protein p53 in HeLa cells upon induction of the model Zn(II) compounds (**1–3**) in different experimental sets was assessed and quantified by the immunofluorescence study. Cells were incubated with the anti-p53 antibody (Santa Cruz Biotechnology, Inc., USA), followed by incubation with the FITC-conjugated secondary antibody (Thermo Fisher Scientific, USA), and then counter-stained with DAPI (Sigma Aldrich, USA) for visualizing the nucleus.

Data availability

We, the authors of this article, confirm that the data will be available on request.

Conflicts of interest

The authors declare that they have no known competing financial interest.

Acknowledgements

The Department of Science, Technology and Biotechnology (DSTBT), West Bengal, India is highly acknowledged for funding and financial support (Grant No. ST/P/S&T/15G-18/2019). The DST-FIST (Level-2; SR/FST/CS-II/2019/96) program is greatly acknowledged for supporting the instrumental facilities in the Department of Chemistry, University of Kalyani. S. S. is thankful to the UGC, New Delhi for offering him a Senior Research Fellowship (SRF).

References

1 F. E. Poynton, S. A. Bright, S. Blasco, D. C. Williams, J. M. Kelly and T. Gunnlaugsson, The Development of Ruthenium(II) Polypyridyl Complexes and Conjugates for *In Vitro* Cellular and *In Vivo* Applications, *Chem. Soc. Rev.*, 2017, **46**, 7706–7756.
2 I. A. Bhat, R. Jain, M. M. Siddiqui, D. K. Saini and P. S. Mukherjee, Water Soluble Pd_8L_4 Self-assembled Molecular Barrel as an Aqueous Carrier for Hydrophobic Curcumin, *Inorg. Chem.*, 2017, **56**, 5352–5360.
3 S. S. Lucky, K. C. Soo and Y. Zhang, Nanoparticles in Photodynamic Therapy, *Chem. Rev.*, 2015, **115**, 1990–2042.
4 W. Ngo, B. Stordy, J. Lazarovits, E. K. Raja, C. L. Etienne and W. C. W. Chan, DNA-Controlled Encapsulation of Small

Molecules in Protein Nanoparticles, *J. Am. Chem. Soc.*, 2020, **142**, 17938–17943.

5 A. Pradhan, S. Haldar, K. B. Mallik, M. Ghosh, M. Bera, N. Sepay, D. Schollmeye, S. K. Ghatake, S. Roy and S. Saha, Mixed Phenoxo and Azido Bridged Dinuclear Nickel(II) and Copper(II) Compounds with *N,N,O*-Donor Schiff Bases: Synthesis, Structure, DNA Binding, DFT and Molecular Docking Study, *Inorg. Chim. Acta*, 2019, **484**, 197–205.

6 H. Ji, W. Wang, O. Qiao and X. Hao, Review of Carrier-Free Self-Assembly of Anticancer Nanodrugs, *ACS Appl. Nano Mater.*, 2024, **7**, 4564–4587.

7 B. Mansoori, A. Mohammadi, S. Davudian, S. Shirjang and B. Baradaran, The Different Mechanisms of Cancer Drug Resistance: A Brief Review, *Adv. Pharm. Bull.*, 2017, **7**, 339–348.

8 A. Ghosh, P. Das, M. R. Gill, P. Kar, M. G. Walker, J. A. Thomas and A. Das, Photoactive Ru^{II}-Polypyridyl Complexes that Display Sequence Selectivity and High-Affinity Binding to Duplex DNA through Groove Binding, *Chem. – Eur. J.*, 2011, **17**, 2089–2098.

9 E. Boisselier and D. Astruc, Gold Nanoparticles in Nanomedicine: Preparations, Imaging, Diagnostics, Therapies And Toxicity, *Chem. Soc. Rev.*, 2009, **38**, 1759–1782.

10 S. Hassan, G. Prakash, A. Ozturk, S. Saghazadeh, M. F. Sohail, J. Seo, M. Dockmeci, Y. S. Zhang and A. Khademhosseini, Evolution and Clinical Translation of Drug Delivery Nanomaterials, *Nano Today*, 2017, **15**, 91–106.

11 P. Starha and Z. Travnicek, Non-Platinum Complexes Containing Releasable Biologically Active Ligands, *Coord. Chem. Rev.*, 2019, **395**, 130–145.

12 L. Zeng, P. Gupta, Y. Chen, E. Wang, L. Ji, H. Chao and Z. S. Chen, The Development of Anti-cancer Ruthenium(II) Complexes: From Single Molecule Compounds to Nanomaterials, *Chem. Soc. Rev.*, 2017, **46**, 5771–5804.

13 S. Wanninger, V. Lorenz, A. Subhan and F. T. Edelmann, Metal Complexes of Curcumin: Synthetic Strategies, Structures and Medicinal Applications, *Chem. Soc. Rev.*, 2015, **44**, 4986–5002.

14 B. Mohan, S. Estalayo-Adrian, D. Umadevi, B. la Cour Poulsen, S. Blasco, G. J. McManus, T. Gunnlaugsson and S. Shanmugaraju, Design, Synthesis, and Anticancer Studies of a *p*-Cymene-Ru(II)-Curcumin Organometallic Conjugate Based on a Fluorescent 4-Amino-1,8-naphthalimide Troger's Base Scaffold, *Inorg. Chem.*, 2022, **61**, 11592–11599.

15 Y. R. Zheng, K. Suntharalingam, T. C. Johnstone and S. J. Lippard, Encapsulation of Pt(IV) Prodrugs within a Pt(II) Cage For Drug Delivery, *Chem. Sci.*, 2015, **6**, 1189–1193.

16 I. Bratsos, S. Jedner, T. Gianferrara and E. Alessio, Ruthenium Anticancer Compounds: Challenges and Expectations, *Chimia*, 2007, **61**, 692–697.

17 C. G. Hartinger, M. A. Jakupec, S. Zorbas-Seifried, B. Kynast, H. Zorbas and B. K. Keppler, A New Redox-Active Anticancer Agent-Preclinical Development and Results of a Clinical Phase I Study in Tumor Patients, *Chem. Biodiversity*, 2008, **5**, 2140–2155.

18 U. Lodemann, R. Einspanier, F. Scharfen, H. Martens and A. Bondzio, Effects of Zinc on Epithelial Barrier Properties and Viability in a Human and a Porcine Intestinal Cell Culture Model, *Toxicol. In Vitro*, 2013, **27**, 834–843.

19 P. Mahato, A. Ghosh, S. K. Mishra, A. Shrivastav, S. Mishra and A. Das, Zn(II) Based Colorimetric Sensor for ATP and Its Use as a Viable Staining Agent in Pure Aqueous Media of pH 7.2, *Chem. Commun.*, 2010, **46**, 9134–9136.

20 W. N. Lipscomb and N. Strater, Recent Advances in Zinc Enzymology, *Chem. Rev.*, 1996, **96**, 2375–2433.

21 P. Ashokkumar, A. H. Ashoka, M. Collot, A. Das and A. S. Klymchenko, A Fluorogenic BODIPY Molecular Rotor as an Apoptosis Marker, *Chem. Commun.*, 2019, **55**, 6902–6905.

22 P. Mahato, A. Ghosh, S. K. Mishra, A. Shrivastav, S. Mishra and A. Das, Zn(II)-Cyclam Based Chromogenic Sensors for Recognition of ATP in Aqueous Solution Under Physiological Conditions and Their Application as Viable Staining Agents for Microorganism, *Inorg. Chem.*, 2011, **50**, 4162–4170.

23 J. L. Qin, W. Y. Shen, Z. F. Chen, L. F. Zhao, Q. P. Qin, Y. C. Yu and H. Liang, Oxoaporphine Metal Complexes (Co^{II}, Ni^{II}, Zn^{II}) With High Antitumor Activity By Inducing Mitochondria-Mediated Apoptosis and S-phase Arrest in HepG2, *Sci. Rep.*, 2017, **7**, 46056.

24 F. X. Wang, M. H. Chen, X. Y. Hu, R. R. Ye, C. P. Tan, L. N. Ji and Z. W. Mao, Ester-Modified Cyclometalated Iridium (III) Complexes As Mitochondria-Targeting Anticancer Agents, *Sci. Rep.*, 2016, **6**, 38954.

25 M. Porchia, M. Pellei, F. Del Bello and C. Santini, Zinc Complexes with Nitrogen Donor Ligands as Anticancer Agents, *Molecules*, 2020, **25**, 5814.

26 M. Pellei, F. Del Bello, M. Porchia and C. Santini, Zinc Coordination Complexes as Anticancer Agents, *Coord. Chem. Rev.*, 2021, **445**, 214088.

27 E. Alessio and L. Messori, Anticancer Drug Candidates Face-to-Face: A Case Story in Medicinal Inorganic Chemistry, *Molecules*, 2019, **24**, 1995.

28 C. Sonkar, S. Sarkar and S. Mukhopadhyay, Ruthenium (II)-Arene Complexes as Anti-Metastatic Agents, and Related Techniques, *RSC Med. Chem.*, 2022, **13**, 22–38.

29 A. Majumder, N. Dutta, S. Dey, P. Sow, A. Samadder, G. Vijaykumar, K. Rangan and M. Bera, A Family of $[Zn_6]$ Complexes from the Carboxylate-Bridge-Supported Assembly of $[Zn_2]$ Building Units: Synthetic, Structural, Spectroscopic, and Systematic Biological Studies, *Inorg. Chem.*, 2021, **60**, 17608–17626.

30 S. Haldar, A. Patra and M. Bera, Exploring The Catalytic Activity of New Water Soluble Dinuclear Copper(II) Complexes Towards The Glycoside Hydrolysis, *RSC Adv.*, 2014, **4**, 62851–62861.

31 S. Haldar, A. Patra, G. Vijaykumar, L. Carrella and M. Bera, Dinuclear and Tetranuclear Complexes of Copper Coordinated by an Anthracene-Based New μ-Bis(tridentate) Ligand: Synthesis, Structure, Spectroscopy and Magnetic Properties, *Polyhedron*, 2016, **117**, 542–551.

32 M. Bera, G. T. Musie and D. R. Powell, Synthesis and Characterization of New Mono- and Heptazinc Complexes with Unusual Amide Coordination Modes, *Inorg. Chem.*, 2009, **48**, 4625–4627.

33 G. C. Giri, A. Patra, G. Vijaykumar, L. Carrella and M. Bera, Hydrolytically Active Tetranuclear $[Ni^{II}_2]_2$ Complexes: Synthesis, Structure, Spectroscopy and Phosphoester Hydrolysis, *RSC Adv.*, 2015, **5**, 99270–99283.

34 S. Haldar, G. Vijaykumar, L. Carrella, S. Batha, G. T. Musie and M. Bera, Inorganic Phosphate and Arsenate within New Tetranuclear Copper and Zinc Complexes: Syntheses, Crystal Structures, Magnetic, Electrochemical, and Thermal Studies, *ACS Omega*, 2017, **2**, 1535–1549.

35 G. C. Giri, S. Haldar, A. K. Ghsoh, P. Chowdhury, L. Carrella, U. Ghosh and M. Bera, New Cyclic Tetranuclear Copper(II) Complexes Containing Quadrilateral Cores: Synthesis, Structure, Spectroscopy and Their Interactions with DNA in Aqueous Solution, *J. Mol. Struct.*, 2017, **1142**, 175–184.

36 A. Majumder, C. Sarkar, I. Das, S. Sk, S. Bandyopadhyay, S. Mandal and M. Bera, Design, Synthesis and Evaluation of a Series of Zinc(II) Complexes of Anthracene-Affixed Multifunctional Organic Assembly as Potential Antibacterial and Antibiofilm Agents against Methicillin-Resistant *Staphylococcus aureus*, *ACS Appl. Mater. Interfaces*, 2023, **15**, 22781–22804.

37 S. Y. van der Zanden, X. Qiao and J. Neefjes, New Insights Into The Activities And Toxicities of The Old Anticancer Drug Doxorubicin, *FEBS J.*, 2021, **288**, 6095–6111.

38 Y. Guan, S. Jiang, W. Ye, X. Ren, X. Wang, Y. Zhang, M. Yin, K. Wang, Y. Tao, J. M. Yang, D. Cao and Y. Cheng, Combined Treatment of Mitoxantrone Sensitizes Breast Cancer Cells To Rapalogs Through Blocking eEF-2K-Mediated Activation of Akt and Autophagy, *Cell Death Dis.*, 2020, **11**, 948.

39 M. Ghanbari-Movahed, T. Kaceli, A. Mondal, M. H. Farzaei and A. Bishayee, Recent Advances in Improved Anticancer Efficacies of Camptothecin Nano-Formulations: A Systematic Review, *Biomedicines*, 2021, **9**, 480.

40 S. Sk, S. Bandyopadhyay, C. Sarkar, I. Das, A. Gupta, M. Sadangi, S. Mondal, M. Banerjee, G. Vijaykumar, J. N. Behera, S. Konar, S. Mandal and M. Bera, Unraveling Multicopper $[Cu_3]$ and $[Cu_6]$ Clusters with Rare μ_3-Sulfato and Linear μ_2-Oxido-Bridges as Potent Antibiofilm Agents against Multidrug-Resistant Staphylococcus aureus, *ACS Appl. Bio Mater.*, 2024, **7**, 2423–2449.

41 A. Patra and M. Bera, Spectroscopic Investigation of New Water Soluble Mn^{II}_2 and Mg^{II}_2 Complexes for the Substrate Binding Models of Xylose/Glucose Isomerases, *Carbohydr. Res.*, 2014, **384**, 87–98.

42 T. S. Kurtikyan, V. A. Hayrapetyan, M. M. Mehrabyan and P. C. Ford, Six-Coordinate Nitrito and Nitrato Complexes of Manganese Porphyrin, *Inorg. Chem.*, 2014, **53**, 11948–11959.

43 B. J. Hathaway, G. Wilkinson, R. G. Gillard and J. A. McCleverty, *Comprehensive Coordination Chemistry*, ed., Pergamon, Oxford, 1987, vol. 2, p. 413.

44 L. Augouy, N. Huby, L. Hirsch, A. van der Lee and P. Gerbier, Molecular Engineering to Improve The Charge Carrier Balance in Single-Layer Silole-Based OLEDs, *New J. Chem.*, 2009, **33**, 1290–1300.

45 N. J. Rose and R. S. Drago, Molecular Addition Compounds of Iodine: An Absolute Method for the Spectroscopic Determination of Equilibrium Constants, *J. Am. Chem. Soc.*, 1959, **81**, 6138–6141.

46 R. Diana and B. Panunzi, The Role of Zinc(II) Ion in Fluorescence Tuning of Tridentate Pincers: A Review, *Molecules*, 2020, **25**, 4984.

47 S. Haldar, N. Dutta, G. Vijaykumar, A. Das, L. Carrella, A. Oliver and M. Bera, Synthesis, Structure and Properties of New Heterometallic Octanuclear $Li_2Na_2Cu_4$ and Decanuclear Li_2Zn_8 Complexes, *Polyhedron*, 2019, **172**, 58–66.

48 P. Portius, B. Peerless, M. Davis and R. Campbell, Homoleptic Poly(nitrato) Complexes of Group 14 Stable at Ambient Conditions, *Inorg. Chem.*, 2016, **55**, 8976–8984.

49 R. Fouad, I. A. Shaaban, T. E. Ali, M. A. Assiri and S. S. Shenouda, Co(II), Ni(II), Cu(II) and Cd(II)-Thiocarbonohydrazone Complexes: Spectroscopic, DFT, Thermal, and Electrical Conductivity Studies, *RSC Adv.*, 2021, **11**, 37726–37743.

50 G. G. Marvin and L. B. Woolaver, Thermal Decomposition of Perchlorates, *Ind. Eng. Chem., Anal. Ed.*, 1945, **17**, 474–476.

51 C. Paquet, T. Lacelle, X. Liu, B. Deore, A. J. Kell, S. Lafreniere and P. R. L. Malenfant, The Role of Amine Ligands in Governing Film Morphology and Electrical Properties of Copper Films Derived from Copper Formate-Based Molecular Inks, *Nanoscale*, 2018, **10**, 6911–6921.

52 A. Addison, T. N. Rao, J. Reedijk, J. van Rijn and G. C. Verschoor, Synthesis, Structure, and Spectroscopic Properties of Copper(II) Compounds Containing Nitrogen-Sulphur Donor Ligands; The Crystal and Molecular Structure of Aqua[1,7- bis(N-methylbenzimidazol-2′-yl)-2,6-dithiaheptane] Copper(II) Perchlorate, *J. Chem. Soc., Dalton Trans.*, 1984, 1349–1356.

53 N. Dutta, S. Haldar, G. Vijaykumar, S. Paul, A. P. Chattopadhyay, L. Carrella and M. Bera, Phosphatase-Like Activity of Tetranuclear Iron(III) and Zinc(II) Complexes, *Inorg. Chem.*, 2018, **57**, 10802–10820.

54 B. Fernandez, I. Fernandez, J. Cepeda, M. Medina-O'Donnell, E. E. Rufino-Palomares, A. Raya-Baron, S. Gomez-Ruiz, A. Perez-Jimenez, J. A. Lupianez, F. J. Reyes-Zurita and A. Rodríguez-Dieguez, Modulating Anticancer Potential by Modifying the Structural Properties of a Family of Zinc Metal−Organic Chains Based on 4-Nitro-1H-pyrazole, *Cryst. Growth Des.*, 2018, **18**, 969–978.

55 A. Tamayo, L. Escriche, J. Casabo, B. Covelo and C. Lodeiro, Synthesis, Complexation and Spectrofluorometric Studies of a New NS_3 Anthracene-Containing Macrocyclic Ligand, *Eur. J. Inorg. Chem.*, 2006, 2997–3004.

56 X. Dai, B. Zhang, W. Zhou and Y. Liu, High-Efficiency Synergistic Effect of Supramolecular Nanoparticles Based on Cyclodextrin Prodrug on Cancer Therapy, *Biomacromolecules*, 2020, **21**, 4998–5007.

57 S. A. Tysoe, R. J. Morgan, A. D. Baker and T. C. Strekas, Spectroscopic Investigation of Differential Binding Modes

of DELTA- and LAMBDA-Ru(bpy)$_2$(ppz)$^{2+}$ with Calf Thymus DNA, *J. Phys. Chem.*, 1993, **97**, 1707–1711.

58 D. Das, A. Banaspati, N. Das, B. Bora, M. K. Raza and T. K. Goswami, Visible Light-Induced Cytotoxicity Studies on Co(II) Complexes having an Anthracene-Based Curcuminoid Ligand, *Dalton Trans.*, 2019, **48**, 12933–12942.

59 F. J. M. Almes and D. Porschke, Mechanism of Intercalation into the DNA Double Helix by Ethidium, *Biochemistry*, 1993, **32**, 4246–4253.

60 J. R. Lakowicz, *Fluorescence Quenching: Theory and Applications. Principles of Fluorescence Spectroscopy*, Kluwer Academic/Plenum Publishers, New York, 1999, pp. 53–127.

61 X. Z. Feng, Z. Yang, L. J. Wang and C. Bai, Investigation of the Interaction between Acridine Orange and Bovine Serum Albumin, *Talanta*, 1998, **47**, 1223–1229.

62 N. Shahabadi, F. Shiri, S. Hadidi, K. Farshadfar, M. Darbemamieh and S. M. Roe, The Role of Both Intercalation and Groove Binding at AT-rich DNA Regions in the Interaction Process of a Dinuclear Cu(I) Complex Probed by Spectroscopic and Simulation Analysis, *J. Mol. Liq.*, 2021, **335**, 116290.

63 W. D. Wilson, F. A. Tanious, D. Ding, A. Kumar, D. W. Boykin, P. Colson, C. Houssier and C. Bailly, Nucleic Acid Interactions of Unfused Aromatic Cations: Evaluation of Proposed Minor-Groove, Major-Groove, and Intercalation Binding Modes, *J. Am. Chem. Soc.*, 1998, **120**, 10310–10321.

64 B. Ray, S. Agarwal, N. Lohani, M. R. Rajeswari and R. Mehrotra, Structural, Conformational and Thermodynamic Aspects of Groove-Directed-Intercalation of Flavopiridol into DNA, *J. Biomol. Struct. Dyn.*, 2016, **34**, 2518–2535.

65 M. K. Sivoňová, M. Vilèková, J. Kliment, S. Mahmood, J. Jureèeková, S. Dušenková, I. Waczulíková, P. Slezák and D. Dobrota, Association of p53 and p21 Polymorphisms with Prostate Cancer, *Biomed. Rep.*, 2015, **3**, 707–714.

66 T. Jiang, C. Zhou, J. Gu, Y. Liu, L. Zhao, W. Li, G. Wang, Y. Li and L. Cai, Enhanced Therapeutic Effect of Cisplatin on the Prostate Cancer in Tumor-Bearing Mice by Transfecting the Attenuated Salmonella Carrying a Plasmid Co-Expressing p53 Gene and mdm2 siRNA, *Cancer Lett.*, 2013, **337**, 133–142.

67 S. Nagata, H. Nagase, K. Kawane, N. Mukae and H. Fukuyama, Degradation of Chromosomal DNA during Apoptosis, *Cell Death Differ.*, 2003, **10**, 108–116.

68 P. R. Walker, L. Kokileva, J. LeBlanc and M. Sikorska, Detection of the Initial Stages of DNA Fragmentation in Apoptosis, *Biotechniques*, 1993, **15**, 1032–1040.

69 A. A. Nazarov, J. Risse, W. H. Ang, F. Schmitt, O. Zava, A. Ruggi, M. Groessl, R. Scopelitti, L. Juillerat-Jeanneret, C. G. Hartinger and P. J. Dyson, Anthracene-Tethered Ruthenium(II) Arene Complexes as Tools to Visualize the Cellular Localization of Putative Organometallic Anticancer Compounds, *Inorg. Chem.*, 2012, **51**, 3633–3639.

70 D. Richardson, E. Tran and P. Ponka, The Potential of Iron Chelators of the Pyridoxal Isonicotinoyl Hydrazone Class as Effective Antiproliferative Agents, *Blood*, 1995, **86**, 4295–4306.

71 C. M. Pfeffer and A. T. K. Singh, Apoptosis: A Target for Anticancer Therapy, *Int. J. Mol. Sci.*, 2018, **19**, 448.

72 H. S. Park, R. Sun, E. J. Lee, J. Kim and N. H. Hur, Triazole-Bridged Zinc Dinuclear Complexes: Mechanochemical Synthesis, Crystal Structure, and Biological Activity, *ACS Omega*, 2022, **7**, 40860–40868.

73 M. Anjomshoa, S. J. Fatemi, M. Torkzadeh-Mahani and H. Hadadzadeh, DNA and BSA Binding Studies and Anticancer Activity Against Human Breast Cancer Cells (MCF-7) of the Zinc(II) Complex Coordinated by 5,6-diphenyl-3-(2-pyridyl)-1,2,4-triazine, *Spectrochim. Acta, Part A*, 2014, **127**, 511–520.

74 M. Narwane, D. P. Dorairaj, Y. L. Chang, R. Karvembu, Y. H. Huang, H. W. Chang and S. C. N. Hsu, Tris-(2-pyridyl)-pyrazolyl Borate Zinc(II) Complexes: Synthesis, DNA/Protein Binding and *In Vitro* Cytotoxicity Studies, *Molecules*, 2021, **26**, 7341.

75 M. K. Bhattacharyya, A. Gogoi, S. Chetry, D. Dutta, A. K. Verma, B. Sarma, A. Franconetti and A. Frontera, Antiproliferative Evaluation and Supramolecular Association in Mn(II) and Zn(II) Bipyridine Complexes: Combined Experimental and Theoretical Studies, *J. Inorg. Biochem.*, 2019, **200**, 110803.

76 J. Li, R. Liu, J. Jiang, X. Liang, L. Huang, G. Huang, H. Chen, L. Pan and Z. Ma, Zinc(II)-Terpyridine Complexes: Substituent Effect on Photoluminescence, Antiproliferative Activity, and DNA Interaction, *Molecules*, 2019, **24**, 4519.

77 R. A. Khan, A. de Almeida, K. Al-Farhan, A. Alsalme, A. Casini, M. Ghazzali and J. Reedijk, Transition-Metal Norharmane Compounds as Possible Cytotoxic Agents: New Insights Based on a Coordination Chemistry Perspective, *J. Inorg. Biochem.*, 2016, **165**, 128–135.

78 M. J. Frisch, G. W. Trucks, H. B. Schlegel, G. E. Scuseria, M. A. Robb, J. R. Cheeseman, J. A. Montgomery, Jr., T. Vreven, K. N. Kudin, J. C. Burant, J. M. Millam, S. S. Iyengar, J. Tomasi, V. Barone, B. Mennucci, M. Cossi, G. Scalmani, N. Rega, G. A. Petersson, H. Nakatsuji, M. Hada, M. Ehara, K. Toyota, R. Fukuda, J. Hasegawa, M. Ishida, T. Nakajima, Y. Honda, O. Kitao, H. Nakai, M. Klene, X. Li, J. E. Knox, H. P. Hratchian, J. B. Cross, C. Adamo, J. Jaramillo, R. Gomperts, R. E. Stratmann, O. Yazyev, A. J. Austin, R. Cammi, C. Pomelli, J. W. Ochterski, P. Y. Ayala, K. Morokuma, G. A. Voth, P. Salvador, J. J. Dannenberg, V. G. Zakrzewski, S. Dapprich, A. D. Daniels, M. C. Strain, O. Farkas, D. K. Malick, A. D. Rabuck, K. Raghavachari, J. B. Foresman, J. V. Ortiz, Q. Cui, A. G. Baboul, S. Clifford, J. Cioslowski, B. B. Stefanov, G. Liu, A. Liashenko, P. Piskorz, I. Komaromi, R. L. Martin, D. J. Fox, T. Keith, M. A. Al-Laham, C. Y. Peng, A. Nanayakkara, M. Challacombe, P. M. W. Gill, B. Johnson, W. Chen, M. W. Wong, C. Gonzalez and J. A. Pople, *Gaussian 03, Revision A.1*, Gaussian, Inc., Pittsburgh, PA, 2003.

79 A. D. Becke, Density-Functional Thermochemistry III: The Role of Exact Exchange, *J. Chem. Phys.*, 1993, **98**, 5648–5652.

80 R. Ditchfield, W. J. Hehre and J. A. Pople, Self-Consistent Molecular-Orbital Methods. IX. An Extended Gaussian-Type

Basis for Molecular-Orbital Studies of Organic Molecules, *J. Chem. Phys.*, 1971, **54**, 724–728.

81 R. Ditchfield, W. J. Hehre and J. A. Pople, Self-Consistent Molecular Orbital Methods. XII. Further Extensions of Gaussian-Type Basis Sets for Use in Molecular Orbital Studies of Organic Molecules, *J. Chem. Phys.*, 1972, **56**, 2257–2261.

82 S. Dey, I. Nagpal, P. Sow, R. Dey, A. Chakrovorty, B. Bhattacharjee, S. Saha, A. Majumder, M. Bera, N. Subbarao, S. Nandi, S. H. Molla, P. Guptaroy, S. K. Abraham, A. R. Khuda-Bukhsh and A. Samadder, Morroniside Interaction with Poly (ADP-ribose) Polymerase Accentuates Metabolic Mitigation of Alloxan-Induced Genotoxicity and Hyperglycaemia: A Molecular Docking Based *In Vitro* and *In Vivo* Experimental Therapeutic Insight, *J. Biomol. Struct. Dyn.*, 2023, 2246585.

83 R. Dey, S. Dey, P. Sow, A. Chakrovorty, B. Bhattacharjee, S. Nandi and A. Samadder, Novel PLGA-Encapsulated-Nanopiperine Promotes Synergistic Interaction of p53/PARP-1/Hsp90 Axis to Combat ALX-Induced-Hyperglycemia, *Sci. Rep.*, 2024, **14**, 9483.

84 A. Paul, J. Das, S. Das, A. Samadder and A. R. Khuda-Bukhsh, Anticancer Potential of Myricanone, a Major Bioactive Component of Myrica Cerifera: Novel Signaling Cascade For Accomplishing Apoptosis, *J. Acupunct. Meridian Stud.*, 2013, **6**, 188–198.

85 D. Sarkar, P. Das, S. Basak and N. Chattopadhyay, Binding Interaction of Cationic Phenazinium Dyes with Calf Thymus DNA: A Comparative Study, *J. Phys. Chem. B*, 2008, **112**, 9243–9249.

86 G. Cohen and H. Einsenberg, Viscosity and Sedimentation Study of Sonicated DNA-Proflavine Complexes, *Biopolymers*, 1969, **8**, 45–55.